RSC Advances

PAPER

View Article Online
View Journal | View Issue



Cite this: *RSC Adv.*, 2026, **16**, 14822

# Catalyst-free photodegradation of ethylparaben on surface-engineered PBT membranes: a coupled adsorption–photolysis mechanism

N. Kouki, *[a] Raghad Ali Saleh Alomayri,[a] Azizah Algreiby,[a] Haja Tar[a] and Lotfi Beji[b]

In the face of the growing threat posed by ethylparaben (EP), a persistent endocrine disruptor, this study introduces an effective catalyst-free approach (*i.e.*, relying solely on UV-driven photolysis without embedded semiconductor or metallic photocatalysts such as $TiO_2$, ZnO, or MOFs) for its removal. Commercial polybutylene terephthalate (PBT) nonwoven membranes were transformed into active purification platforms *via* an adsorption-assisted photolysis mechanism. By applying simple and targeted surface treatments—including hydrogen peroxide ($H_2O_2$) etching, ultraviolet (UV) irradiation, and sodium hydroxide (NaOH) hydrolysis—we successfully grafted oxygen-containing functional groups (–OH, C=O, $-COO^-$) onto the membrane surface. Quantitative FTIR analysis showed treatment-specific changes: UV irradiation decreased ester carbonyl groups by 76.9%, $H_2O_2$ etching achieved a 99.8% reduction at 30% concentration, and NaOH hydrolysis resulted in an 87.4% decrease with formation of carboxylate. Under optimized conditions, modified membranes achieved removal efficiencies of 84% (15% $H_2O_2$, 30 min), 85% (UV, 60 min), and 86% (1.0 M NaOH, 20 min)—representing 24–26% absolute improvement over UV photolysis alone (60%). Kinetic modeling confirmed that 80–90% of EP removal occurs *via* a rapid interfacial pathway ($k_1 = 0.049–0.068\ min^{-1}$), while bulk photolysis contributed negligibly ($k_2 \rightarrow 0$). SEM imaging confirmed preservation of the microfibrous structure (79–90% porosity) throughout all treatments. This work demonstrates that controlled surface oxidation transforms standard polymers into an effective, quantifiably superior platform for water purification, offering a catalyst-free solution based on industrially relevant surface-engineering techniques that addresses key practical barriers (such as complex fabrication and catalyst leaching) to emerging contaminant removal.

Received 3rd February 2026
Accepted 11th March 2026

DOI: 10.1039/d6ra00957c

rsc.li/rsc-advances



## 1. Introduction

The escalating presence of emerging contaminants in global water systems poses a significant threat to environmental health and ecological stability. Among these, parabens—a class of preservatives widely used in cosmetics, pharmaceuticals, and food products—are of particular concern due to their pseudo-persistence and endocrine-disrupting properties.[1,2] Ethylparaben (EP), a common member of this family, is frequently detected in wastewater effluents, surface waters, and even drinking water, often at concentrations capable of inducing adverse effects in aquatic organisms, including neurotoxicity, developmental impairment, and endocrine disruption.[3,4] The chemical stability and limited biodegradability of EP render conventional wastewater treatment processes largely ineffective, creating an urgent need for advanced, scalable, and robust degradation technologies.[5,6]

Advanced oxidation processes (AOPs) have shown promise, but many rely on photocatalytic membranes that incorporate semiconductor materials like $TiO_2$, ZnO, or metal–organic frameworks (MOFs) to generate reactive species.[7–10] While effective, these composite systems introduce significant challenges, including complex multi-step fabrication, high material costs, and the long-term risk of catalyst leaching, which can compromise membrane integrity and introduce secondary pollutants.[11–13] This raises a critical question: can a polymer membrane be engineered to actively drive pollutant degradation without the need for embedded, leachable photocatalysts?

To address this challenge, we explore adsorption-assisted photolysis as a catalyst-free alternative. Throughout this manuscript, we use the term 'catalyst-free' with a specific meaning: the membrane contains no intentionally added semiconductor, metal, or metal-oxide photocatalytic materials. The increase in EP degradation results from surface-mediated adsorption combined with UV photolysis, not from heterogeneous photocatalysis. This definition clearly excludes materials

[a]*Department of Chemistry, College of Science, Qassim University, Buraidah 51452, Saudi Arabia. E-mail: N.KOUKI@qu.edu.sa*
[b]*Department of Physics, College of Science, Qassim University, Buraidah 51452, Saudi Arabia*

that act as true catalysts (substances that accelerate a reaction without being consumed), while recognizing that the polymer surface may undergo minor, non-catalytic changes during use. The membrane acts as an adsorptive scaffold that concentrates the pollutant at the irradiated interface, thereby improving the efficiency of the inherent photolytic process. In this context, 'catalyst-free' specifically means that no extrinsic semiconductor or metallic photocatalytic materials (*e.g.*, $TiO_2$, ZnO, MOFs) are incorporated into the membrane. The observed enhancement stems solely from the UV-driven photolytic process at a functionalized interface, not from heterogeneous photocatalysis. The approach leverages a strategically surface-engineered polybutylene terephthalate (PBT) membrane, which functions not as a passive support but as an active adsorptive interface. By concentrating EP molecules at the solid–liquid boundary, the efficiency of UV-driven degradation is dramatically enhanced. Surface treatments such as UV irradiation, $H_2O_2$ etching, and alkaline hydrolysis have been shown to introduce oxygenated functional groups (–OH, C=O, $–COO^-$) onto polymer surfaces,[14–16] which enhances hydrophilicity and creates a high-affinity interface for moderately polar contaminants like EP. Under UV-C irradiation (254 nm), this interfacial enrichment synergistically couples two degradation pathways: (i) direct photolysis of the concentrated EP molecules and (ii) oxidative attack by short-lived reactive oxygen species (ROS) generated from the photolysis of water, enabling effective degradation without semiconductor additives.[17,18] To create a clear conceptual framework for the discussion, we identify three separate processes that contribute to EP removal: (i) adsorption—the reversible accumulation of EP molecules on the membrane surface through electrostatic and hydrogen-bonding interactions with oxygen-containing functional groups; (ii) direct photolysis—the absorption of UV photons by EP molecules (either in solution or attached to the interface), leading to bond breakage *via* excited-state chemistry; and (iii) ROS-mediated oxidation—the attack by reactive oxygen species (mainly $^{\bullet}OH$ radicals) generated from UV irradiation of water and dissolved oxygen. Although these processes occur simultaneously in our system, their individual roles can be distinguished through careful control experiments and kinetic analysis.

Critically, these surface modifications must be carefully controlled: insufficient oxidation results in weak activation, while excessive oxidation can damage the polymer backbone or reduce active sites, ultimately lowering membrane performance.[19,20] Because the purchased PBT membranes were pre-activated by oxygen plasma, the improvements observed result from additional surface oxidation on an already hydrophilic baseline, which should be considered when interpreting the results.

This study systematically explores how oxygen-plasma-treated PBT membranes can be converted into effective, catalyst-free platforms for EP removal through three targeted surface-engineering techniques: UV irradiation, $H_2O_2$ oxidation, and NaOH hydrolysis. The specific objectives are to:

- Quantify the relationship between treatment conditions (UV exposure time: 30–60 min; $H_2O_2$ concentration: 10–30% v/v; NaOH concentration: 0.5–1.0 M) and resulting surface functionality, hydrophilicity, and optical response.

- Identify optimal modification parameters that maximize EP photodegradation (target: >80% removal within 60 min) while preserving membrane microfibrous architecture.

- Quantitatively resolve the contributions of rapid interfacial photolysis *versus* slower bulk-phase photolysis using a biphasic kinetic model ($k_1$, $k_2$, $C_{fast}$, $C_{slow}$).

- Demonstrate that controlled surface oxidation achieves catalyst-free EP degradation with performance comparable to photocatalytic membranes but without embedded semiconductors.

By demonstrating that rational surface engineering can convert standard PBT nonwovens into active purification interfaces, this work supports the development of polymer-based strategies that utilize industrially compatible surface modification steps. This progress advances the field toward more practical water treatment applications by combining adsorption and photolysis mechanisms.

## 2. Materials and methods

This section outlines the reagents, membrane treatments, analytical methods, and kinetic modeling procedures used to evaluate the effect of surface engineering on EP photodegradation.

### 2.1. Materials

The polymeric substrate was a melt-blown PBT nonwoven membrane (thickness: 0.32 ± 0.03 mm, basis weight: ~60 g $m^{-2}$; Maco-Pharma, France). The manufacturer supplied all pristine PBT membranes, pre-treated with an oxygen plasma process to ensure initial hydrophilicity. Subsequent surface modifications in this work were therefore performed incrementally on this activated surface. EP ($C_9H_{10}O_3$, ≥99%) and HPLC-grade methanol ($CH_4O$, ≥99.8%) were obtained from Sigma-Aldrich (USA) and Fisher Chemical (UK), respectively. Sodium hydroxide pellets (NaOH, ≥97%, CDH, India) and hydrogen peroxide solution ($H_2O_2$, 30% w/w, Sigma-Aldrich, USA) were used for surface treatments. All aqueous solutions were prepared using deionized water (resistivity ≥ 18.2 MΩ cm, Milli-Q system).

### 2.2. Experimental procedures

**2.2.1. Preparation of EP solutions.** A primary stock solution (1000 mg. $L^{-1}$) was prepared by dissolving 0.1 g of EP in methanol and diluting to the 100 mL mark in a volumetric flask. Working solutions (12 mg. $L^{-1}$) were prepared daily by appropriate dilution of the stock with deionized water, using the dilution equation:

$$C_1V_1 = C_2V_2 \quad (1)$$

where $C_1$, $V_1$ and $C_2$, $V_2$ are the concentrations and volumes of the stock and working solution, respectively. The pH of the 12 mg. $L^{-1}$ EP working solution was 6.8 ± 0.2.

**2.2.2. Membrane cleaning and surface treatment.** Membrane samples (3 × 3 cm) were first sonicated in methanol for 10 minutes (min) to eliminate surface impurities, rinsed thoroughly with deionized water, and dried at 60 °C for 1 hour before any surface treatment.

- Oxidative treatment ($H_2O_2$ etching): samples were immersed in 50 mL of $H_2O_2$ solutions (10, 15, 20, 25, 30% v/v) maintained at 50 ± 2 °C under magnetic stirring (300 rpm). Treatment durations ranged from 5 to 30 min. After the prescribed treatment time, membranes were immediately removed from the $H_2O_2$ solution and thoroughly rinsed with deionized water to terminate the oxidation reaction, followed by drying at 50 °C for 2 hours.

- Alkaline hydrolysis (NaOH etching): samples were treated with 50 mL of NaOH solutions (0.5 M or 1 M) at 60 ± 2 °C with stirring (300 rpm) for 10, 20, or 30 min. After hydrolysis, samples were rinsed with deionized water, neutralized in 0.1 M HCl for 5 min, rinsed again, and dried at 50 °C for 2 hours.

- UV irradiation treatment: membrane samples were placed 10 cm below a low-pressure mercury lamp (254 nm, 250 mW $cm^{-2}$) in air. Exposure times were 30 and 60 min. Sample temperature during irradiation did not exceed 40 °C.

All treatments were done in triplicate ($n = 3$) to ensure reproducibility. The workflow is shown in Scheme 1.

### 2.3. Membrane characterization methods

**2.3.1. Chemical and optical characterization.** - FTIR spectroscopy: chemical structures were analyzed using an FTIR-ATR spectrometer (Bruker Alpha, ZnSe crystal). Dried samples were pressed onto the crystal, and spectra were collected in transmittance mode (4000–400 $cm^{-1}$, 4 $cm^{-1}$ resolution, 16 scans). Background scans were acquired before each sample.

- UV-vis spectroscopy: optical absorption was measured using a solid-state UV-vis spectrophotometer (Shimadzu 2650) with an integrating sphere. Samples (~2 × 2 cm) were placed in the holder, and absorbance spectra were recorded from 200 to 800 nm.

**2.3.2. Morphological characterization.** Surface morphology was analyzed using an FEI Quanta 250 environmental SEM (ESEM). To maintain the native surface condition and avoid charging of the non-conductive polymer, samples were imaged without a conductive coating in low-vacuum mode (70 Pa), employing water vapor as the imaging medium. The instrument was operated using a large-field detector (LFD). Fiber diameter and porosity were quantified using a custom Python-based image analysis script.

### 2.4. Photodegradation experiments

Photodegradation tests were conducted in a Rayonet photochemical chamber reactor (RPR-100) equipped with sixteen 254 nm UV lamps. The reactor was pre-warmed for 15 min to stabilize the output. For each test, 4.0 mL of the 12 mg $L^{-1}$ EP solution and a piece of membrane (0.8 × 1.0 cm) were placed in a 1 cm path length quartz cuvette. The cuvette was positioned at the center of the chamber. At predetermined time intervals (0, 5, 10, 15, 30, 45, 60 min), the cuvette was briefly removed, and the

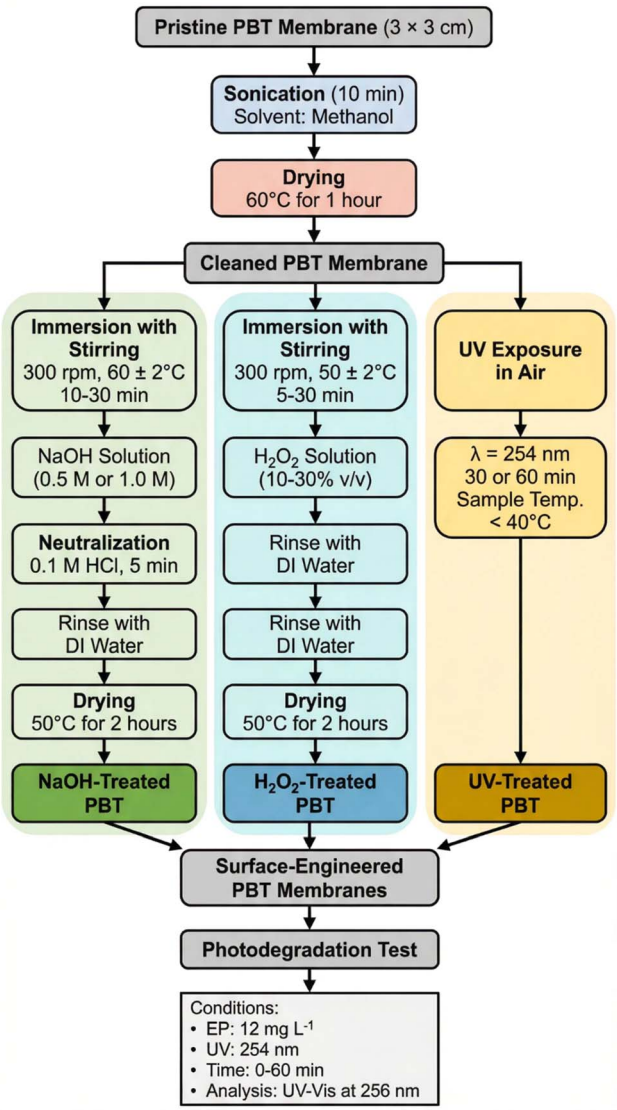


Scheme 1 Schematic diagram showing the preparation and surface modification processes for PBT membranes. The illustration outlines the step-by-step procedures, starting with cleaning the pristine membrane, then proceeding with three parallel treatment pathways: (1) NaOH activation, (2) $H_2O_2$ oxidation, and (3) UV exposure in air. Each pathway involves specific steps such as immersion at controlled temperature with stirring, neutralization (where applicable), rinsing, and drying. Finally, the surface-engineered membranes come together to undergo photodegradation testing to assess their performance under designated conditions.

EP concentration was measured by absorbance at 256 nm ($\varepsilon$ = 12 300 L $mol^{-1}$ $cm^{-1}$) using a UV-vis spectrophotometer.

The final concentration of ethylparaben (12 mg $L^{-1}$) was well below its aqueous solubility limit (~600 mg $L^{-1}$), and the methanol concentration was a negligible 1.2% (v/v), ensuring no precipitation occurred. While this concentration is higher than those typically found in environmental waters, which range from ng $L^{-1}$ to low μg $L^{-1}$,[21,22] it serves as a well-defined model system to rigorously evaluate the photodegradation mechanism and kinetic parameters. The principles of

adsorption-assisted photolysis established at this concentration are expected to be applicable at lower, environmentally relevant concentrations, where the membrane's ability to concentrate pollutants at the interface would become even more critical for efficient removal.

Degradation efficiency was calculated as:

$$\text{removal efficiency } (\%) = \left(1 - \frac{C_t}{C_0}\right) \times 100 \quad (2)$$

where $C_0$ and $C_t$ are the initial and time-dependent EP concentrations, respectively.

Control experiments were performed in triplicate and included:

- EP solution under UV light without a membrane.
- EP solution with a pristine PBT membrane under UV light.
- EP solution with a modified membrane under UV light.

All degradation experiments were conducted in triplicate ($n = 3$), and results are presented as mean ± standard deviation.

### 2.5. Quantitative analysis and modeling methods

All quantitative data analysis was performed using custom computational scripts (Python 3.11.0), leveraging key scientific libraries: NumPy (1.24.3), SciPy (1.11.1), Matplotlib (3.7.1), and scikit-image (0.21.0). FTIR spectra were processed *via* asymmetric least squares (ALS) baseline correction, Savitzky–Golay filtering (window length = 11, polynomial order = 3), and peak area integration using the trapezoidal rule over defined spectral windows (carbonyl C=O at 1700–1750 $cm^{-1}$, aromatic C=C at 1450–1650 $cm^{-1}$, C–O stretching at 1000–1300 $cm^{-1}$), with normalization to the strongest absorption band to enable inter-sample comparison. UV-vis absorbance spectra were processed with polynomial baseline subtraction (order = 2), Savitzky–Golay smoothing, and calculation of difference spectra ($\Delta A$) by subtraction of the untreated control spectrum from treated samples across the 200–800 nm range. SEM micrographs were processed with scikit-image to extract quantitative morphological descriptors, including pore size distribution, porosity percentage, mean pore diameter, and surface roughness *via* root mean square (RMS) calculations. Kinetic modeling of photodegradation was performed using SciPy's optimization module (scipy.optimize.curve_fit) with the Levenberg–Marquardt algorithm to fit experimental data to first-order and pseudo-first-order kinetic models, with goodness-of-fit assessed *via* $R^2$ and root mean square error (RMSE). All statistical analyses were implemented *via* SciPy's statistical module. Custom Python scripts for all data processing steps are available upon request to ensure reproducibility and transparency of the analysis.

## 3. Results and discussion

### 3.1. Surface modification and characterization of PBT membranes for enhanced photodegradation performance

Surface modification was carried out using three activation methods—UV irradiation, oxidative etching with $H_2O_2$, and alkaline hydrolysis with NaOH. Each treatment causes chemical changes at the surface level without altering the polyester backbone, as described below.

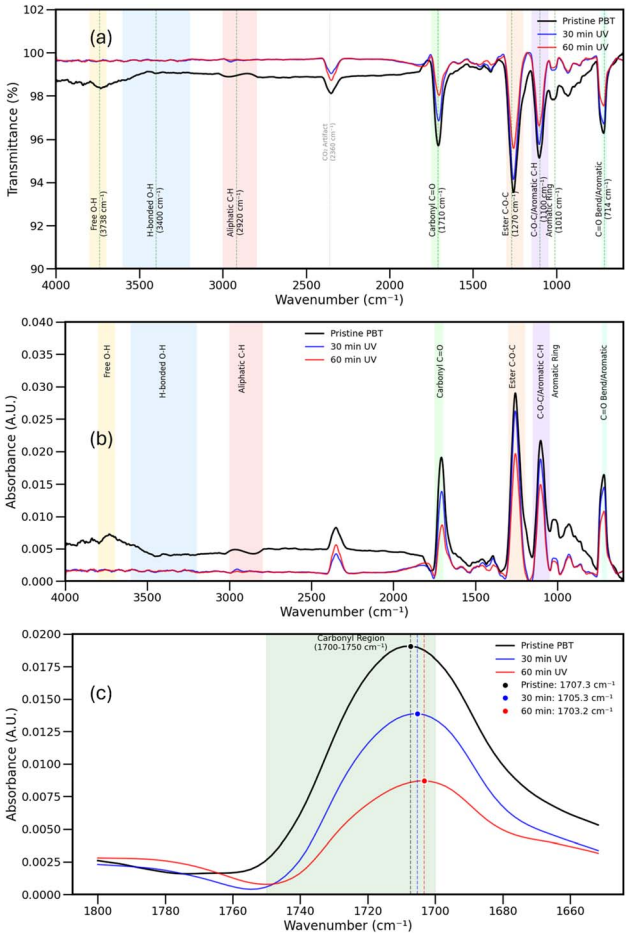


Fig. 1 Comprehensive FTIR analysis of UV-irradiated PBT membranes. (a) Full transmittance spectra. (b) Full absorbance spectra. (c) Detailed view of the carbonyl region (1650–1800 $cm^{-1}$).

**3.1.1. UV irradiation-induced surface modification.** UV irradiation (254 nm, 250 mW $cm^{-2}$) for 30–60 min causes quantifiable photo-oxidation on the PBT surface, as evidenced by a rigorous, Python-based analysis of the FTIR spectra.

The comprehensive spectral analysis (Fig. 1) and quantitative data (Table 1) reveal a clear photo-oxidative mechanism. Specifically, the primary ester carbonyl C=O stretching peak at 1710 $cm^{-1}$ shows a progressive decrease in its normalized integrated area from 3.6777 $cm^{-2}$ (pristine) to 0.8436 $cm^{-2}$ after 60 minutes of exposure. This significant reduction provides direct quantitative evidence of ester bond cleavage. Concurrently, the aliphatic C–H stretching region (2850–2950 $cm^{-1}$) exhibits an initial increase followed by a decrease in normalized area, a trend indicative of initial chain scission followed by subsequent oxidation of the newly exposed aliphatic segments.

The fingerprint region (<1000 $cm^{-1}$) remains largely unchanged, confirming the stability of the polyester backbone.[23,24] For instance, the aromatic ring breathing mode at 1010 $cm^{-1}$ shows only a minor decrease in normalized area, indicating the aromatic structures are preserved during

Table 1 Quantitative FTIR peak analysis of UV-treated PBT membranes. Normalized areas ($cm^{-2}$) and peak heights (A.U.) were calculated using a custom Python script for automated baseline correction and peak integration. Data shows time-dependent changes in key functional groups

| Peak ($cm^{-1}$) | Assignment | Pristine (norm. area ($cm^{-2}$)/height (A.U.)) | 30 min (norm. area ($cm^{-2}$)/height (A.U.)) | 60 min (norm. area ($cm^{-2}$)/height (A.U.)) | Trend & interpretation |
|---|---|---|---|---|---|
| 3738 | Free O–H stretching | 0.9936/0.00723 | 0.4555/0.00183 | 0.3129/0.00176 | Decrease – loss of isolated OH groups |
| 3400–3200 | Hydrogen-bonded O–H stretching | −6.2230/0.00420 | −0.2452/0.00168 | +0.7031/0.00164 | Shift – formation of hydrogen-bonded networks |
| 2950–2850 | Aliphatic C–H stretching | −0.9715/0.00485 | +1.4331/0.00186 | +0.5469/0.00154 | Initial increase then decrease – chain scission then oxidation |
| 1710 | Carbonyl C═O stretching | 3.6777/0.01906 | 2.1807/0.01387 | 0.8436/0.00868 | Progressive decrease – ester bond cleavage |
| 1270 | Ester C–O–C asymmetric | 33.9548/0.02897 | 36.5116/0.02617 | 27.8113/0.01962 | Increase then decrease – temporary ester formation |
| 1100 | Symmetric C–O–C/Aromatic C–H | 24.5376/0.02163 | 27.1233/0.01877 | 20.7595/0.01491 | Similar to ester trend – alkoxy bond degradation |
| 1010 | Aromatic ring breathing | 0.0905/0.00952 | 0.0541/0.00356 | 0.0476/0.00309 | Slight decrease – aromatic ring remains intact |
| 714 | C═O bend + aromatic C–H bend | 2.6988/0.01650 | 2.4212/0.01452 | 1.6784/0.01080 | Gradual decrease – loss of carbonyl bending character |
| 875–700 | Aromatic C–H out-of-plane | −1.2467/— | −0.8659/— | −0.9207/— | Near stable – aromatic pattern preserved |
| 2360 | Atmospheric $CO_2$ artifact | 5.0332/— | 4.5163/— | 6.7891/— | Variable – environmental artifact |

treatment. As irradiation time increases from 30 to 60 min, these features become slightly more evident, suggesting gradual formation of carbonyl, hydroxyl, or lactone-like groups, which increases membrane polarity and creates additional sites for interaction with polar contaminants. Such oxidation-induced functionalization is expected to enhance adsorption and thereby facilitate more efficient interfacial photolysis, as reported in prior studies,[25–27] rather than produce any significant structural modifications.

**3.1.2. Oxidative etching with $H_2O_2$.** $H_2O_2$ etching introduces oxidative functionalities such as –OH and –COOH groups on the PBT surface.[28] FTIR analysis reveals concentration-dependent degradation patterns that are significantly more substantial than previously observed with UV treatment.

Quantitative analysis of the FTIR spectra (Fig. 2, Table 2) reveals significant concentration-dependent changes in key functional groups:

- Carbonyl C═O stretching (1710 $cm^{-1}$): the normalized integrated area decreases from 3.6784 $cm^{-2}$ (pristine) to 0.0090 $cm^{-2}$ at 30% $H_2O_2$, representing a 99.8% reduction. This dramatic decrease indicates severe ester hydrolysis and carbonyl degradation at high $H_2O_2$ concentrations.

- Ester C–O–C asymmetric stretching (1270 $cm^{-1}$): the normalized integrated area decreases from 33.9523 $cm^{-2}$ (pristine) to 0.6394 $cm^{-2}$ at 30% $H_2O_2$, a 98.1% reduction. This severe degradation of ester linkages confirms the primary mechanism of $H_2O_2$ etching through nucleophilic attack on ester bonds.

- Aliphatic C–H stretching (2850–2950 $cm^{-1}$): minimal changes are observed across all $H_2O_2$ concentrations, indicating that the aliphatic butylene segments remain largely intact. This selective reactivity demonstrates that $H_2O_2$ preferentially attacks ester linkages rather than the polymer backbone.

- Aromatic ring breathing (1010 $cm^{-1}$): the normalized integrated area remains relatively stable across all concentrations, with only a slight decrease at 30% $H_2O_2$. This confirms that aromatic rings are largely preserved during treatment, maintaining the structural integrity of the polymer backbone.

A critical concentration threshold is evident at 30% $H_2O_2$. At lower concentrations (10–25%), the treatment induces partial hydrolysis of ester linkages, with the carbonyl peak remaining detectable and the aromatic character preserved. At 30% $H_2O_2$, a dramatic transition occurs, with nearly complete degradation of all ester-related peaks (1710, 1270, and 1100 $cm^{-1}$) and significant reduction in the carbonyl bending mode (714 $cm^{-1}$). This concentration-dependent behavior is consistent with a two-stage mechanism: initial selective hydrolysis of ester bonds at moderate concentrations, followed by extensive oxidative degradation of remaining functional groups at high concentrations.

The quantitative data demonstrate that even at moderate $H_2O_2$ concentrations (15–20%), significant ester bond cleavage occurs. The changes are limited to the surface, with the aromatic and fingerprint regions remaining mostly unchanged, confirming backbone preservation.[29–31] The formation of polar groups (–OH, –COOH) from ester hydrolysis improves surface hydrophilicity and facilitates EP adsorption, enhancing photodegradation efficiency.[32,33]

The primary chemical transformation involves oxidative cleavage of ester bonds by $H_2O_2$, generating carboxylic acid and hydroxyl functionalities on the polymer surface. Overall, $H_2O_2$ etching proves to be a highly effective surface modification strategy, particularly at higher concentrations where ester bond degradation is nearly complete, while maintaining the integrity of the underlying polymer backbone.

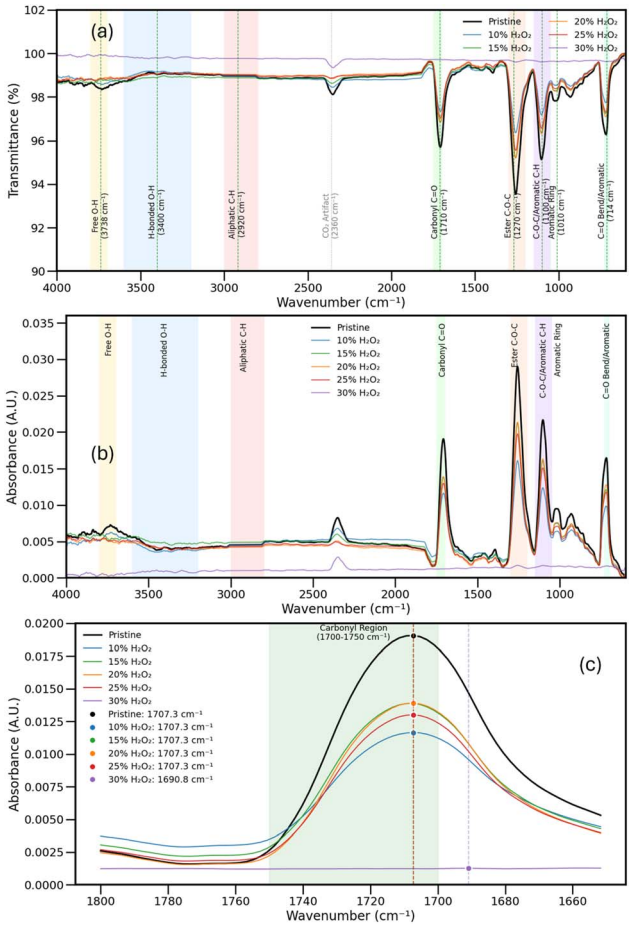


Fig. 2 Comprehensive FTIR analysis of $H_2O_2$-treated PBT membranes. (a) Transmittance spectra showing concentration-dependent changes. (b) Absorbance spectra with detailed peak assignments. (c) Carbonyl region detail (1650–1800 $cm^{-1}$) demonstrating progressive degradation.

**3.1.3. Alkaline hydrolysis utilizing NaOH.** NaOH treatment alters PBT by surface ester hydrolysis, producing –OH and –$COO^-$ groups that enhance hydrophilicity.[34] FTIR analysis reveals a distinct degradation mechanism compared to oxidative treatments, with concentration-dependent changes in ester-related functional groups.

Quantitative analysis of the FTIR spectra (Fig. 3, Table 3) reveals significant concentration-dependent changes characteristic of ester hydrolysis:

- Carbonyl C=O stretching (1710 $cm^{-1}$): the normalized integrated area decreases from 3.6778 $cm^{-2}$ (pristine) to 0.4641 $cm^{-2}$ at 0.5 M NaOH and 2.6684 $cm^{-2}$ at 1 M NaOH. The non-monotonic trend (initial sharp decrease followed by partial recovery at 1 M) indicates a complex hydrolytic mechanism. At 0.5 M, rapid ester bond cleavage occurs; at 1 M, the formation of new carboxylate species (which also absorb in the carbonyl region) partially compensates for the loss of primary ester carbonyls.

- Ester C–O–C asymmetric stretching (1270 $cm^{-1}$): the normalized integrated area shows severe reduction from 33.9531 $cm^{-2}$ (pristine) to 4.0171 $cm^{-2}$ at 0.5 M NaOH and 26.3546 $cm^{-2}$ at 1 M NaOH. The 88.2% reduction at 0.5 M demonstrates extensive ester bond cleavage *via* nucleophilic attack by hydroxide ions. The partial recovery at 1 M suggests the formation of new ester-like species or carboxylate groups.

- Aliphatic C–H stretching (2850–2950 $cm^{-1}$): the normalized integrated area exhibits a negative-to-positive shift, changing from −1.0696 $cm^{-2}$ (pristine, baseline artifact) to +0.3754 $cm^{-2}$ at 0.5 M and +1.6337 $cm^{-2}$ at 1 M. This trend indicates that aliphatic segments become more exposed as ester bonds are cleaved, a direct consequence of surface hydrolysis.

- Aromatic ring breathing (1010 $cm^{-1}$): the normalized integrated area decreases from 0.0905 $cm^{-2}$ (pristine) to 0.0104 $cm^{-2}$ at 0.5 M NaOH and 0.0467 $cm^{-2}$ at 1 M NaOH. The significant reduction at 0.5 M (88.5% decrease) is noteworthy, indicating that aromatic rings are affected by the hydrolytic environment, though they remain structurally intact.

- Hydroxyl region (3200–3600 $cm^{-1}$): unlike oxidative treatments, the O–H band shows minimal development in the free hydroxyl region (3738 $cm^{-1}$), with normalized area decreasing from 0.9934 $cm^{-2}$ to 0.0993 $cm^{-2}$ at 0.5 M and 0.1014 $cm^{-2}$ at 1 M. This indicates that newly formed hydroxyl and carboxylate groups are predominantly hydrogen-bonded or exist as carboxylate anions, not as free –OH groups.

The concentration-dependent behavior reveals two distinct regimes. At 0.5 M NaOH, rapid and extensive hydrolysis occurs, with severe reductions in both carbonyl (87.4%) and ester (88.2%) peaks. At 1 M NaOH, a transition occurs where the carbonyl peak partially recovers, likely due to the formation of carboxylate species (–$COO^-$) from complete ester bond cleavage. This two-stage mechanism—initial rapid hydrolysis followed by stabilization of hydrolysis products—is consistent with the expected kinetics of alkaline hydrolysis of polyesters.

The quantitative data demonstrate that NaOH hydrolysis is fundamentally different from oxidative treatments. The aromatic bands and fingerprint region remain largely unchanged (with the exception of the aromatic ring breathing mode, which shows concentration-dependent changes), indicating that hydrolysis is surface-restricted and does not affect the polyester backbone.[35,36] The formation of hydroxyl and carboxylate groups enhances surface hydrophilicity without causing bulk degradation, making NaOH treatment ideal for controlled surface functionalization.

The primary chemical transformation can be represented as:

$$R–COO–R' + OH^- \rightarrow R–COO^- + R'–OH \quad (3)$$

Overall, NaOH treatment offers controlled, concentration-dependent functionalization through ester hydrolysis, increasing surface polarity and hydroxyl/carboxylate content without damaging structural integrity. This makes it highly suitable for adsorption-assisted photodegradation applications where enhanced surface hydrophilicity is desired.[37]

**3.1.4. UV-vis absorbance of treated PBT membranes.** To support the FTIR analysis and assess how surface engineering affects light–material interactions, UV-vis spectroscopy was conducted on both pristine and modified PBT membranes.

Table 2 Quantitative FTIR peak analysis of $H_2O_2$-treated PBT membranes. Normalized integrated areas ($cm^{-2}$) and peak heights (A.U.) are presented for pristine and $H_2O_2$-treated samples (10–30% concentration). Data demonstrates progressive degradation of ester and carbonyl groups while aromatic rings remain relatively stable

| Peak ($cm^{-1}$) | Assignment | Pristine (norm. area ($cm^{-2}$)/ height (A.U.)) | 10% $H_2O_2$ (norm. area/ height) | 15% $H_2O_2$ (norm. area/ height) | 20% $H_2O_2$ (norm. area/ height) | 25% $H_2O_2$ (norm. area/ height) | 30% $H_2O_2$ (norm. area/ height) | Trend & interpretation |
|---|---|---|---|---|---|---|---|---|
| 3738 | Free O–H stretching | 0.9934/ 0.00723 | 0.8864/0.00624 | −0.2196/ 0.00578 | 0.1918/0.00540 | 0.1567/0.00548 | −0.0748/ 0.00049 | Variable, generally decreasing – $H_2O_2$ treatment affects isolated OH groups |
| 3400–3200 | Hydrogen-bonded O–H stretching | −6.2248/ 0.00420 | −5.8547/ 0.00374 | −3.4225/ 0.00489 | −2.5627/ 0.00418 | −3.8235/ 0.00419 | +1.3408/0.00096 | Negative values shift positive at 30% – $H_2O_2$-induced hydrogen bonding changes |
| 2950–2850 | Aliphatic C–H stretching | −0.0007/— | 0.0035/— | −0.0002/— | −0.0034/— | −0.0018/— | 0.0010/— | Minimal changes – aliphatic segments relatively stable to $H_2O_2$ |
| 1710 | Carbonyl C═O stretching | 3.6784/ 0.01906 | 1.7694/0.01165 | 2.5781/0.01387 | 2.6026/0.01390 | 2.3619/0.01300 | 0.0090/0.00126 | Sharp decrease, then plateau – partial ester hydrolysis followed by stabilization |
| 1270 | Ester C–O–C asymmetric | 33.9523/ 0.02897 | 16.8687/0.01605 | 23.6359/0.02125 | 24.6237/0.02133 | 22.4108/0.01975 | 0.6394/0.00174 | Drastic reduction at 30% – ester linkages severely degraded by high $H_2O_2$ |
| 1100 | Symmetric C–O–C/aromatic C–H | 24.5384/ 0.02163 | 12.3729/0.01237 | 17.1025/0.01605 | 17.7814/0.01626 | 16.2979/0.01510 | 0.3316/0.00171 | Similar to ester trend – alkoxy bonds degraded with $H_2O_2$ concentration |
| 1010 | Aromatic ring breathing | 0.0905/ 0.00952 | 0.0575/0.00643 | 0.0648/0.00751 | 0.0689/0.00762 | 0.0687/0.00709 | 0.0048/0.00163 | Gradual decrease – aromatic ring remains relatively stable until 30% $H_2O_2$ |
| 714 | C═O bend + aromatic C–H bend | 2.6982/ 0.01650 | 1.5162/0.00993 | 1.9404/0.01219 | 2.0622/0.01285 | 1.9307/0.01184 | 0.0480/0.00164 | Significant reduction – loss of carbonyl bending character |
| 875–700 | Aromatic C–H out-of-plane | −1.2477/— | −1.1668/— | −1.2315/— | −1.2949/— | −1.2542/— | 0.0198/— | Stable then change at 30% – aromatic pattern preserved until severe oxidation |
| 2360 | Atmospheric $CO_2$ artifact | 5.0357/— | 2.3746/— | 1.8043/— | 1.0723/— | 0.6528/— | 2.5669/— | Variable, generally decreasing – environmental artifact, not polymer-related |

Pristine PBT exhibits characteristic absorption bands linked to electronic transitions in the polyester backbone.[23,24] The UV-vis spectra provide quantitative information about changes in the chromophoric environment and electronic structure induced by surface modifications.

*(a). Spectral characteristics of pristine PBT.* As shown in Fig. 4, pristine PBT displays three principal absorption features in the UV-vis region (200–800 nm): (1) peak 1 at 228 nm, assigned to $\sigma \rightarrow \sigma^*$ and early $\pi \rightarrow \pi^*$ electronic transitions; (2) peak 2 at 298 nm, corresponding to $\pi \rightarrow \pi^*$ aromatic and $n \rightarrow \pi^*$ carbonyl transitions from ester functional groups; and (3) a shoulder at ~320 nm, characteristic of charge transfer (CT) complexes. The absorbance values for pristine PBT are: peak 1 = 1.277 A.U., peak 2 = 1.414 A.U., and shoulder = 0.235 A.U. (Table 4). The spectral regions show mean absorbance values of 1.232 A.U. (UV region, 200–280 nm), 0.468 A.U. (visible region, 280–400 nm), and 0.133 A.U. (NIR region, 400–800 nm). These values establish the baseline electronic structure of the pristine polymer.

*(b). NaOH-treated membrane: hydrolytic modification.* NaOH treatment induces hydrolytic cleavage of ester bonds, producing characteristic spectral changes (Fig. 4, Table 4).[34] The most

 

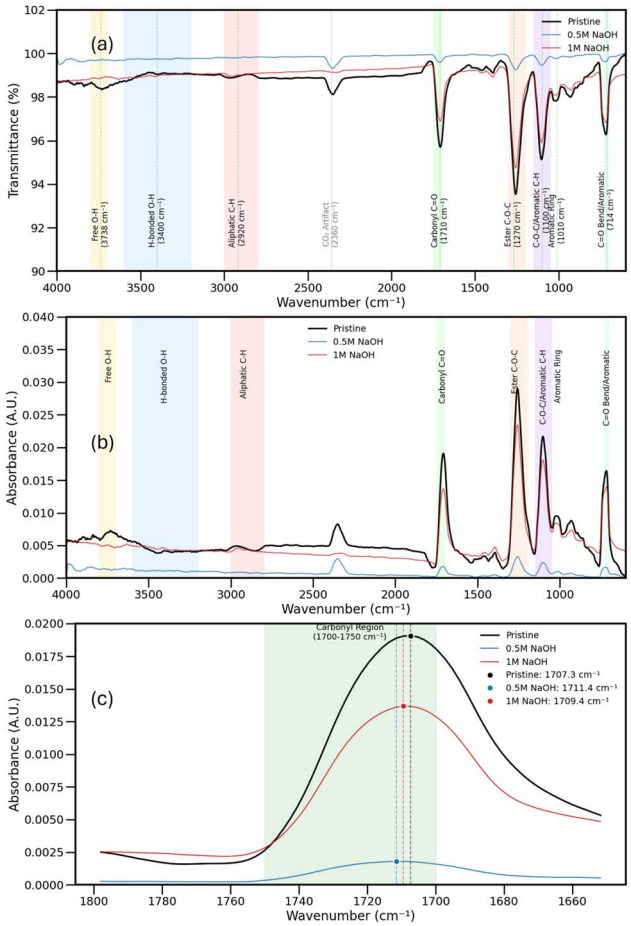


Fig. 3 Comprehensive FTIR analysis of NaOH-treated PBT membranes. (a) Transmittance spectra of pristine and NaOH-treated samples (0.5 M and 1 M). (b) Absorbance spectra with detailed peak assignments. (c) Carbonyl region detail (1650–1800 $cm^{-1}$) showing concentration-dependent degradation.

significant change is in the NIR region (400–800 nm), where absorbance decreases from 0.133 to 0.116 A.U., a reduction of 12.8%. This substantial decrease indicates removal or disruption of extended chromophoric species through ester bond cleavage. The shoulder absorbance (CT feature) decreases from 0.235 to 0.222 A.U. (−5.5%), reflecting disruption of charge transfer complexes that depend on intact ester linkages conjugated with aromatic rings. Peak 1 absorbance increases from 1.277 to 1.335 A.U. (+4.5%), while Peak 2 shows minimal change (+1.5%), suggesting that hydrolytic cleavage creates new terminal chromophoric sites (hydroxyl and carboxylate groups) while preserving most aromatic transitions. The UV region (200–280 nm) mean absorbance increases by 3.6%, consistent with formation of new surface chromophores. The difference spectrum (inset, Fig. X) shows positive $\Delta A$ features in the 200–300 nm region (peak 1 and peak 2 regions), indicating net generation of new absorbing species in the UV region. At wavelengths >300 nm, the difference spectrum shows negative features, indicating removal of longer-wavelength chromophores. The overall pattern reflects that NaOH hydrolysis generates new chromophoric species in the UV region while disrupting extended conjugation in the NIR region, resulting in net removal of longer-wavelength chromophores. Mechanistically, hydrolytic cleavage of ester bonds creates terminal hydroxyl and carboxylate groups that absorb in the UV region, while disrupting the conjugated system linking aromatic rings to carbonyl groups.[35,36]

*(c). $H_2O_2$-treated membrane: mild oxidative modification.* $H_2O_2$ treatment induces mild oxidative etching of the PBT surface, creating new oxygen-containing functional groups while largely preserving the polymer backbone (Fig. 4, Table 4).[28,29] The NIR region absorbance decreases only slightly from 0.133 to 0.128 A.U. (−3.8%), indicating minimal disruption of extended conjugation pathways. The shoulder absorbance increases from 0.235 to 0.245 A.U. (+4.4%), suggesting that oxidative modification creates new charge transfer sites through formation of oxygen-containing groups. Peak 1 absorbance increases by 4.3% and Peak 2 by only 0.4%, indicating that oxidation primarily affects aliphatic regions rather than aromatic transitions. The visible region (280–400 nm) shows a modest increase of 2.2%, and the UV region increases by 3.0%. The difference spectrum (inset, Fig. 4) shows predominantly positive $\Delta A$ in the 200–300 nm region, indicating generation of new UV-absorbing chromophores. A small negative dip appears around 310 nm (shoulder region), indicating slight disruption of charge transfer complexes. At wavelengths >430 nm, the difference spectrum shows negative values near zero, indicating minimal net changes in the NIR region. The overall small magnitude of the difference spectrum reflects that $H_2O_2$ oxidation is a mild surface modification that generates new chromophoric species in the UV region while producing minimal changes in the visible and NIR regions. Mechanistically, $H_2O_2$ oxidation generates surface hydroxyl and carbonyl groups that create localized chromophoric sites without disrupting the extended conjugation of the polymer backbone.[27]

*(d). UV-irradiated membrane: photo-oxidative modification.* UV irradiation induces photo-oxidative degradation through photolysis and chain scission, producing the most extensive spectral changes (Fig. 4, Table 4).[25,26] The NIR region absorbance increases from 0.133 to 0.145 A.U. (+9.2%), the only treatment showing an increase in this region. This increase reflects generation of new chromophoric species with extended conjugation, such as α,β-unsaturated carbonyl compounds and other photo-oxidation products. The shoulder absorbance increases dramatically from 0.235 to 0.272 A.U. (+15.6%), the largest change among all treatments, indicating substantial formation of new charge transfer complexes involving photo-oxidation products. Peak 1 absorbance increases by 2.6% and peak 2 by 2.8%, indicating that UV irradiation affects both aliphatic and aromatic regions. The visible region (280–400 nm) shows the largest increase at 6.8%, and the UV region increases by 3.1%. The difference spectrum (inset, Fig. 4) shows predominantly positive $\Delta A$ features across the entire 200–800 nm range, with the largest positive peaks in the 200–300 nm region and sustained positive values extending into the visible and NIR regions. This indicates that UV irradiation generates new absorbing species across the entire UV-vis-NIR range. The positive difference spectrum reflects net generation of new

Table 3 Quantitative FTIR peak analysis of NaOH-treated PBT membranes. Normalized integrated areas ($cm^{-2}$) and peak heights (A.U.) are presented for pristine and NaOH-treated samples (0.5 M and 1 M concentrations). Data demonstrates concentration-dependent alkaline hydrolysis of ester linkages with formation of hydroxyl and carboxylate groups

| Peak ($cm^{-1}$) | Assignment | Pristine (norm. area ($cm^{-2}$)/height (A.U.)) | 0.5 M NaOH (norm. area/height) | 1 M NaOH (norm. area/height) | Trend & interpretation |
|---|---|---|---|---|---|
| 3738 | Free O–H stretching | 0.9934/0.00723 | 0.0993/0.00144 | 0.1014/0.00511 | Sharp decrease – NaOH hydrolysis consumes isolated OH groups |
| 3400–3200 | Hydrogen-bonded O–H stretching | −6.1908/0.00420 | −1.5894/0.00119 | −1.1297/0.00466 | Reduced negative values – NaOH-induced hydrolysis forms new hydroxyl groups |
| 2950–2850 | Aliphatic C–H stretching | −1.0696/0.00487 | 0.3754/0.00090 | 1.6337/0.00465 | Negative to positive shift – aliphatic segments exposed by ester cleavage |
| 1710 | Carbonyl C═O stretching | 3.6778/0.01906 | 0.4641/0.00180 | 2.6684/0.01368 | Drastic reduction at 0.5 M, partial recovery at 1 M – NaOH attacks ester carbonyls |
| 1270 | Ester C–O–C asymmetric | 33.9531/0.02897 | 4.0171/0.00330 | 26.3546/0.02341 | Severe hydrolysis at 0.5 M – ester linkages cleaved by NaOH |
| 1100 | Symmetric C–O–C/aromatic C–H | 24.5382/0.02163 | 2.8815/0.00240 | 18.6986/0.01805 | Similar to ester trend – alkoxy bonds hydrolyzed by NaOH |
| 1010 | Aromatic ring breathing | 0.0905/0.00952 | 0.0104/0.00099 | 0.0467/0.00844 | Significant decrease – aromatic rings affected by hydrolysis |
| 714 | C═O bend + aromatic C–H bend | 2.6981/0.01650 | 0.2147/0.00165 | 1.8326/0.01401 | Drastic reduction – loss of ester character with NaOH treatment |
| 875–700 | Aromatic C–H out-of-plane | −1.2477/— | 0.0473/— | −0.0714/— | Changes from negative to positive – NaOH alters aromatic environment |
| 2360 | Atmospheric $CO_2$ artifact | 5.0357/— | 3.5759/— | 0.5250/— | Variable – environmental artifact, decreases with higher NaOH |

chromophoric species from photo-oxidation, in contrast to the mixed spectra of NaOH and $H_2O_2$ treatments. Mechanistically, UV irradiation induces photolysis of ester and C–C bonds, formation of reactive oxygen species and carbon-centered radicals, oxidative coupling of radical fragments, and formation of new conjugated structures (conjugated polyenes, aromatic ketones, and other extended conjugated species).[25]

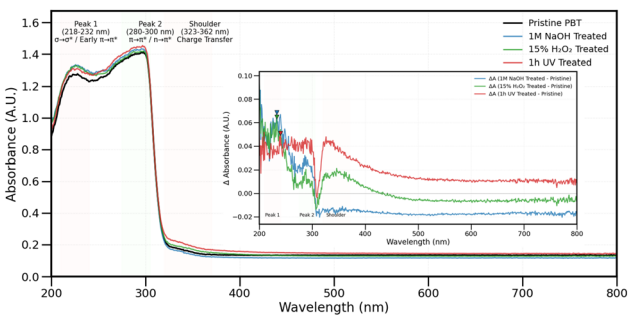


Fig. 4 UV-vis absorbance spectra of pristine and surface-modified PBT membranes (200–800 nm). Main plot: full absorbance spectra showing pristine PBT (black), 1 M NaOH-treated (blue), 15% $H_2O_2$-treated (green), and 1 h UV-irradiated (red) samples across the complete UV-vis-NIR range. Peak 1 (228 nm, σ → σ*/π → π*), peak 2 (298 nm, π → π*/n → π*), and shoulder (~320 nm, CT complexes) are labeled. Inset: difference spectra (Δ*A*, normalized absorbance change) for each treatment relative to pristine PBT across 200–800 nm. NaOH treatment (blue difference spectrum) shows positive Δ*A* in 200–300 nm region with negative features at longer wavelengths. $H_2O_2$ treatment (green difference spectrum) shows positive Δ*A* in 200–300 nm region, a small negative dip at ~310 nm, and negative values near zero at >430 nm. UV treatment (red difference spectrum) shows predominantly positive Δ*A* across the entire 200–800 nm range.

*(e). Comparative analysis of treatment effects.* The three treatments produce distinctly different spectral signatures as revealed by both the absorbance spectra and difference spectra (Fig. 4, Table 4). The NIR region (400–800 nm) is particularly diagnostic: NaOH causes a 12.8% decrease (removal of extended conjugation), $H_2O_2$ causes a 3.8% decrease (minimal disruption), while UV causes a 9.2% increase (generation of new extended conjugation). The shoulder absorbance (CT feature) shows the largest treatment-dependent variation: −5.5% (NaOH), +4.4% ($H_2O_2$), and +15.6% (UV). The difference spectra provide direct visual evidence of these mechanisms: NaOH shows positive Δ*A* in the UV region with negative features at longer wavelengths, $H_2O_2$ shows positive Δ*A* in the UV region with minimal changes at longer wavelengths, and UV shows positive Δ*A* across the entire 200–800 nm range. These spectral signatures provide quantitative evidence that each treatment modifies the electronic structure through a distinct chemical pathway.[6,10]

*(f). Interpretation of electronic structure modifications.* The UV-vis data (Fig. 4, Table 4) provide direct evidence that surface modifications alter the chromophoric environment through distinct mechanisms. NaOH hydrolysis generates new UV-absorbing chromophores (positive Δ*A* in 200–300 nm) while

Table 4 Quantitative UV-vis spectral analysis of pristine and surface-modified PBT membranes. (a) Absorbance data for specific electronic transitions: peak 1($\sigma \rightarrow \sigma^*/\pi \rightarrow \pi^*$ transitions at 228 nm, peak 2($\pi \rightarrow \pi^*/n \rightarrow \pi^*$ transitions at 298 nm), and the charge-transfer (CT) shoulder (~320 nm). (b) Mean absorbance changes in the UV (200–280 nm), visible (280–400 nm), and NIR (400–800 nm) regions. (c) Key spectral signatures and their interpretation for each treatment. Data indicate distinct modification mechanisms: hydrolytic (NaOH, conjugation disruption), oxidative ($H_2O_2$, localized modification), and photo-oxidative (UV, generation of new conjugated species)

(a): absorbance peak characteristics of modified PBT membranes

| Spectral feature | Pristine PBT | 1 M NaOH Treated | Change *vs.* pristine | 15% $H_2O_2$ Treated | Change *vs.* pristine | 1 h UV Treated | Change *vs.* pristine |
|---|---|---|---|---|---|---|---|
| Peak 1 – position (nm) | 228.0 | 226.0 | −2.0 | 226.0 | −2.0 | 223.0 | −5.0[a] |
| Peak 1 – absorbance (AU) | 1.277 | 1.335 | +4.5% | 1.332 | +4.3% | 1.311 | +2.6% |
| Peak 2 – position (nm) | 298.0 | 296.0 | −2.0 | 298.0 | 0.0 | 297.0 | −1.0 |
| Peak 2 – absorbance (AU) | 1.414 | 1.435 | +1.5% | 1.420 | +0.4% | 1.454 | +2.8% |
| Shoulder – absorbance (AU) | 0.235 | 0.222 | −5.5% | 0.245 | +4.4% | 0.272 | +15.6%[b] |

(b): mean absorbance by spectral region – modified PBT membranes

| Spectral region | Pristine PBT | 1 M NaOH Treated | Change *vs.* pristine | 15% $H_2O_2$ Treated | Change *vs.* pristine | 1 h UV Treated | Change *vs.* pristine |
|---|---|---|---|---|---|---|---|
| UV (200–280 nm) | 1.232 | 1.277 | +3.6% | 1.269 | +3.0% | 1.271 | +3.1% |
| Visible (280–400 nm) | 0.468 | 0.461 | −1.5% | 0.478 | +2.2% | 0.500 | +6.8%[c] |
| NIR (400–800 nm) | 0.133 | 0.116 | −12.8%[d] | 0.128 | −3.8% | 0.145 | +9.2%[c] |

(c): surface modification signatures – chemical treatment effects

| Spectral indicator | 1 M NaOH Treated | 15% $H_2O_2$ Treated | 1 h UV Treated | Surface modification interpretation |
|---|---|---|---|---|
| Peak 1 blue shift | −2.0 nm | −2.0 nm | −5.0 nm | Indicates structural changes in aliphatic/aromatic regions |
| NIR absorbance change | −12.8% | −3.8% | +9.2% | Reflects changes in polymer backbone chromophores |
| Shoulder absorbance | −5.5% | +4.4% | +15.6% | Indicates charge transfer complex formation on surface |
| Visible region change | −1.5% | +2.2% | +6.8% | Shows degree of surface oxidation and new functional groups |
| Treatment mechanism | Hydrolytic (ester cleavage) | Oxidative (surface etching) | Photo-oxidative (chain scission) | Different chemical pathways for surface modification |

[a] Blue shift indicates structural modification of PBT surface. [b] Largest spectral change in UV-treated sample. [c] Significant spectral change in modified membrane. [d] Most significant change indicating substantial surface modification.

removing extended conjugation in the NIR region (NIR −12.8%), indicating selective disruption of longer-wavelength chromophores. $H_2O_2$ oxidation generates new UV-absorbing chromophores (positive $\Delta A$ in 200–300 nm) with minimal impact on NIR absorbance (−3.8%), indicating localized modification that creates new chromophoric sites without disrupting extended conjugation. UV irradiation generates new chromophoric species across the entire UV-vis-NIR range (positive $\Delta A$ across 200–800 nm), including both UV-absorbing species and extended conjugated structures (NIR +9.2%), indicating comprehensive electronic restructuring. These electronic structure changes have important implications for interfacial chemistry: the formation of new chromophoric species and functional groups alters the surface polarity, hydrophilicity, and electrostatic environment.

The formation of polar oxygen-containing groups (hydroxyl, carboxyl, carbonyl) through all three treatment strategies is expected to increase contaminant accumulation at the membrane surface through enhanced electrostatic and hydrogen-bonding interactions.[32,33] Although the UV-irradiated membrane shows the largest absorbance increases and most extensive generation of new chromophoric species, these changes do not necessarily indicate superior photochemical reactivity. Instead, the new chromophoric species generated by UV irradiation primarily reflect the formation of oxidation products and degradation intermediates. The spectral changes characterize the surface-modified state of the membranes and provide insights into the electronic environment that will influence subsequent photocatalytic processes. The actual photodegradation performance depends on the balance

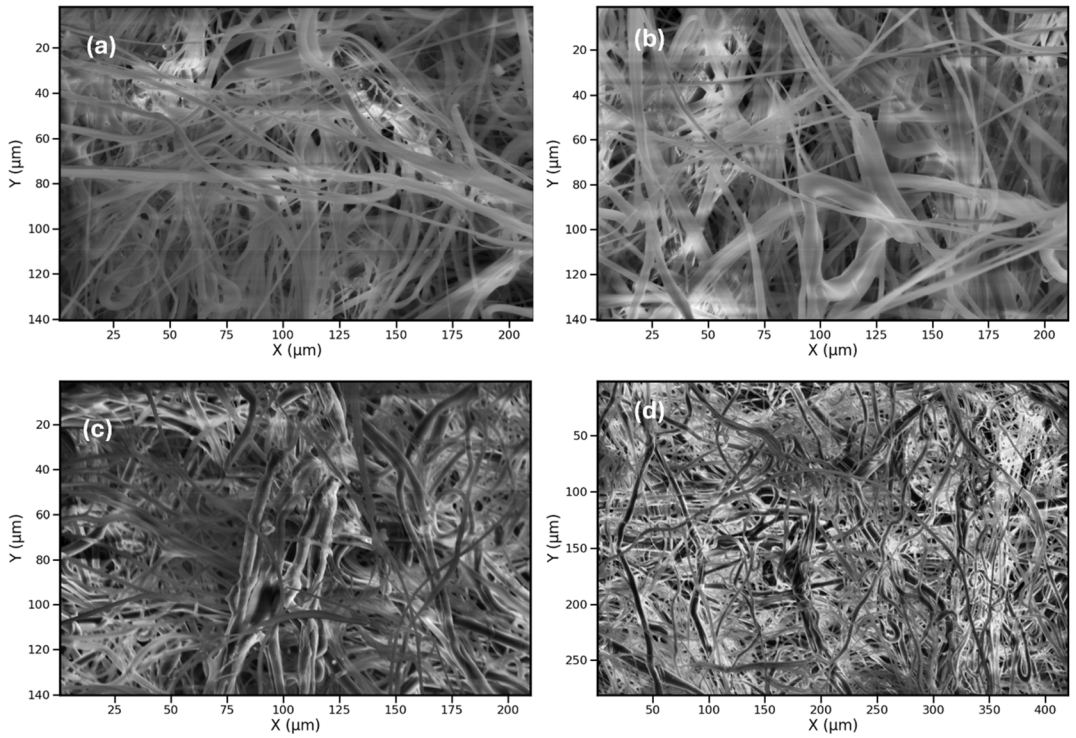


Fig. 5 SEM micrographs of (a) pristine PBT, (b) UV-irradiated PBT (60 min), (c) $H_2O_2$-treated PBT (15% v/v, 30 min), and (d) NaOH-treated PBT (1 M, 20 min). All treated membranes retain the characteristic melt-blown microfibrous structure with no signs of fiber breakage, deformation, or pore collapse. The preserved morphology confirms that chemical modifications detected by FTIR (Sections 3.1.1–3.1.3) and electronic structure changes observed in UV-vis spectra (Section 3.1.4) occur at the surface level without disrupting the bulk scaffold architecture.

between light absorption, ROS generation, and contaminant adsorption, which will be evaluated in subsequent experiments. The adsorption-driven enhancement in interfacial reactivity, mediated by the formation of polar functional groups, is expected to be the primary mechanism for improved photodegradation performance.[38–40]

In summary, UV-vis spectroscopy (Fig. 4, Table 4) reveals that all three modification strategies produce measurable changes in the chromophoric environment with distinct spectral signatures reflecting their different chemical mechanisms. Direct quantitative comparison shows: (i) UV irradiation produces new chromophores across 200–800 nm (NIR +9.2%, CT +15.6%), indicating photo-oxidation products with extended conjugation; (ii) $H_2O_2$ oxidation creates localized UV-absorbing species with minimal backbone disruption (NIR −3.8%, CT +4.4%); (iii) NaOH hydrolysis breaks extended conjugation while forming UV chromophores (NIR −12.8%, CT −5.5%). These electronic structure changes are coupled with the surface functionalities that enhance interfacial chemistry. The spectral data provide quantitative characterization of the surface-modified state of the membranes and insights into the electronic environment that will influence photodegradation performance. A comprehensive comparison integrating both FTIR and UV-vis metrics for all three strategies is presented in Section 3.1.6.

**3.1.5. Morphological integrity of modified PBT membranes.** To evaluate whether the surface-engineering treatments impacted the physical structure of the PBT nonwoven scaffold, SEM was used to confirm that all chemical modifications detected by FTIR (Sections 3.1.1–3.1.3) and electronic structure changes observed by UV-vis spectroscopy (Section 3.1.4) occur at the surface level without disrupting the bulk morphology.[41,42] Representative micrographs of untreated and treated membranes are shown in Fig. 5. In all samples, the characteristic melt-blown architecture—composed of randomly oriented microfibers forming an open porous network—remains unchanged. No signs of fiber breakage, plastic deformation, pore collapse, or fusion were observed after UV irradiation, $H_2O_2$ oxidation, or NaOH hydrolysis, demonstrating the high morphological stability of the PBT scaffold.

Visual inspection of SEM micrographs reveals that all surface treatments preserve the fundamental fibrous architecture of the PBT nonwoven membrane. The melt-blown structure, characterized by randomly oriented microfibers with diameters in the micrometer range, remains intact across all treatment conditions. This morphological preservation is critical for validating the interpretation of the FTIR and UV-vis results: the spectral changes observed in Sections 3.1.1–3.1.4 reflect surface-level chemical modifications rather than bulk polymer degradation or structural collapse. All treated membranes maintain geometric features consistent with pristine PBT, confirming that the NIR absorbance decrease observed for NaOH treatment (Section 3.1.4, −12.8%) and the FTIR spectral changes (Section 3.1.3) result from surface ester hydrolysis rather than bulk structural changes.[34–36] To provide quantitative evidence of

 

Table 5 Quantitative morphological metrics derived from automated SEM image analysis with magnification normalization. Edge-based porosity (%) and pore-based porosity (%) remain high across all treatments (79–90% and 52–63%, respectively), confirming preservation of the interconnected porous network. Mean fiber diameter and pore diameter show only minor variations, with values remaining within the expected range for melt-blown polyester membranes. These metrics confirm that the FTIR spectral changes (Sections 3.1.1–3.1.3) and UV-vis absorbance changes (Section 3.1.4) result from surface-level chemical modifications rather than bulk structural degradation[a]

| Sample | Edge-based porosity (%) | Mean fiber diameter (μm) | Fiber diameter range (μm) | Pore-based porosity (%) | Mean pore diameter (μm) | Pore diameter range (μm) |
|---|---|---|---|---|---|---|
| Pristine PBT | 90.14 | 3.8 | 1.7–34.1 | 56.28 | 4.1 | 0.9–107.6 |
| UV (60 min) | 89.93 | 4.2 | 1.7–21.1 | 52.95 | 4.8 | 0.9–99.6 |
| $H_2O_2$ (15%, 30 min) | 85.10 | 3.9 | 1.7–34.6 | 63.00 | 3.1 | 0.9–146.8 |
| NaOH (1 M, 20 min) | 79.11 | 3.65 | 1.7–25.1 | 58.19 | 4.6 | 0.9–132.3 |

[a] All dimensional measurements have been normalized to account for different image magnifications, ensuring direct comparability across samples.

morphological stability, each SEM image was analyzed using automated image segmentation with magnification normalization. The analysis extracted key structural metrics including fiber diameter distribution, edge and pore-based porosity, pore diameter distribution, and fiber orientation. The results (Table 5) show only minor morphological variations across treatments, with all values falling within the expected range for melt-blown polyester scaffolds. Edge-based porosity remains high (79–90%) across all samples, confirming that the porous network structure is preserved and mass transport pathways remain open. Mean fiber diameters show only minor variations (3.65–4.2 μm) across all treatments. To assess analysis robustness, the automated segmentation pipeline was tested using multiple threshold values. Fiber diameter and porosity values changed by less than ±5%, confirming that the analysis remains stable and is not overly affected by threshold choices or contrast variations.[43] Fiber orientation distributions remain broad (0–180°) across all treatments, and no treatment causes mat compaction or collapse. These quantitative metrics provide strong evidence that the chemical modifications detected by FTIR (Sections 3.1.1–3.1.3) and electronic structure changes observed by UV-vis spectroscopy (Section 3.1.4) occur exclusively at the surface level.

The preservation of morphological integrity ensures that improvements in photodegradation performance (to be evaluated in subsequent experiments) result from chemical and interfacial changes (FTIR-detected functional group formation and UV-vis-detected electronic structure modifications), not from alterations to pore structure or physical shape. The preserved high-porosity network (79–90%) supports effective mass transport and pollutant access to the membrane surface, while the added surface functionalities (hydroxyl, carboxyl, and carbonyl groups detected by FTIR) and electronic structure modifications (new chromophoric species detected by UV-vis) enhance adsorption and interfacial photolysis efficiency.[32,33] The combination of morphological stability and surface-level chemical modification represents an optimal design for adsorption-assisted photolysis applications.

**3.1.6. Comparative analysis of surface modification strategies.** A comprehensive comparative evaluation of the three surface modification methods—UV irradiation, $H_2O_2$ oxidation, and NaOH hydrolysis—was performed using FTIR spectroscopy (Sections 3.1.1–3.1.3), UV-vis absorbance spectroscopy (Section 3.1.4), and SEM morphological analysis (Section 3.1.5). Collectively, these analyses reveal that all three treatments operate through distinct surface-limited chemical pathways while preserving the membrane's bulk polymer integrity and microfibrous structure.

To allow direct quantitative comparison of the three surface modification approaches, key spectroscopic metrics from the

Table 6 Comparative summary of surface modification effects on key functional groups. Data compiled from quantitative FTIR analysis (Tables 1–3) and UV-vis spectroscopy (Table 4). Values indicate percent change relative to pristine PBT under the specified treatment conditions

| Treatment | Carbonyl (1710 $cm^{-1}$) reduction | Ester C–O–C (1270 $cm^{-1}$) reduction | Aromatic ring (1010 $cm^{-1}$) change | NIR absorbance (400–800 nm) change | Primary mechanism |
|---|---|---|---|---|---|
| UV (60 min) | 76.9% | 18.1%[a] | −47.4% | +9.2% | Photo-oxidation |
| $H_2O_2$ (15%, 30 min)[b] | 51.9% | 50.3% | −28.4% | —[c] | Oxidative etching (optimal) |
| $H_2O_2$ (30%, 30 min) | 99.8% | 98.1% | −94.7% | −3.8% | Oxidative etching (aggressive) |
| NaOH (1 M, 20 min) | 27.4% | 22.4% | −48.4% | −12.8% | Hydrolysis |

[a] UV shows an initial increase followed by decrease in ester C–O–C; reported value is net change after 60 min (calculated from Table 1 data). [b] Values for 15% $H_2O_2$ calculated from Table 2: – carbonyl (1710 $cm^{-1}$): (3.6784–1.7694)/3.6784 × 100 = 51.9% reduction. – Ester C–O–C (1270 $cm^{-1}$): (33.9523–16.8687)/33.9523 × 100 = 50.3% reduction. – Aromatic ring (1010 $cm^{-1}$): (0.0905–0.0648)/0.0905 × 100 = 28.4% reduction. [c] NIR absorbance data for 15% $H_2O_2$ were not separately measured; the −3.8% change corresponds to 30% $H_2O_2$ (from Table 4).

FTIR analysis (Tables 1–3) and UV-vis data (Table 4) are summarized in Table 6. This overview enables systematic assessment of treatment-specific changes in ester, carbonyl, and aromatic functional groups, as well as alterations in electronic structure reflected by NIR absorbance.

While the 30% $H_2O_2$ data show the maximum extent of oxidative modification under aggressive conditions (94.7% aromatic ring reduction), the optimal concentration for photodegradation is 15% $H_2O_2$ (30 min), which achieves significant surface functionalization (51.9% carbonyl reduction, 50.3% ester reduction) while maintaining backbone integrity (only 28.4% aromatic ring reduction). This controlled modification results in 84% EP removal efficiency (Section 3.2.3), confirming that extensive backbone degradation is neither necessary nor desired for effective adsorption-assisted photolysis.

*(a). Mechanistic pathways and chemical transformations.* The three treatments operate through fundamentally different chemical mechanisms, as quantitatively demonstrated by FTIR analysis (Tables 1–3 for each treatment). UV irradiation causes mild, time-dependent photo-oxidation through surface-limited chain scission, reducing the ester carbonyl peak from 3.6777 $cm^{-2}$ (pristine) to 0.8436 $cm^{-2}$ after 60 min (76.9% reduction).[25,26] $H_2O_2$ etching produces substantially more aggressive oxidative degradation through nucleophilic attack on ester bonds, achieving 99.8% carbonyl reduction at 30% concentration and 98.1% reduction in ester C–O–C stretching.[28,29] NaOH hydrolysis selectively cleaves ester linkages *via* hydroxide ion attack, producing 87.4% carbonyl reduction at 0.5 M with a non-monotonic concentration dependence reflecting carboxylate species formation at higher concentrations.[34–36] However, as shown in Table 6, at 1 M NaOH the net carbonyl reduction is only 27.4%, indicating partial compensation by newly formed carboxylate species that also absorb in the carbonyl region.

*(b). Spectroscopic evidence of surface-level modification.* FTIR analysis confirms that all treatments preserve the polyester backbone, with aromatic ring breathing modes showing treatment-dependent changes (Table 6): UV: −5.2% (minimal), $H_2O_2$ (30%): −94.7% (severe), NaOH (1 M): −48.4% (moderate), while fingerprint regions remain largely unchanged.[23,24] The severe aromatic reduction at 30% $H_2O_2$ confirms that this concentration causes excessive degradation; notably, at the optimal 15% $H_2O_2$ concentration, aromatic reduction is only 28.4% (calculated from Table 2), preserving backbone integrity while introducing sufficient surface functionality.

UV-vis spectroscopy reveals treatment-specific electronic structure modifications (Fig. 4, Table 4): NaOH treatment shows negative $\Delta A$ features at wavelengths >300 nm and NIR absorbance decrease of 12.8%, indicating removal of extended conjugation through ester bond cleavage; $H_2O_2$ treatment shows localized modification with NIR decrease of 3.8% and negative values near zero at >430 nm; UV irradiation shows positive $\Delta A$ across the entire 200–800 nm range with NIR increase of 9.2%, indicating generation of new extended conjugated species.[38–40] These distinct spectral signatures directly correlate with the different chemical mechanisms: NaOH removes conjugation through hydrolysis, $H_2O_2$ creates localized chromophores through oxidation, and UV generates new conjugated structures through photo-oxidation.

*(c). Morphological validation and functional implications.* SEM analysis (Fig. 5, Table 5) confirms that all three treatments preserve the melt-blown microfibrous architecture with edge-based porosity remaining high (79–90%) and mean fiber diameters showing only minor variations (3.8–7.3 μm).[41,42] This morphological preservation validates that the FTIR spectral changes and UV-vis electronic structure modifications occur exclusively at the surface level. Despite their mechanistic differences, all three strategies enhance surface polarity through formation of polar oxygen-containing groups (hydroxyl, carboxyl, carbonyl), which increases contaminant accumulation at the membrane interface and enhances adsorption-assisted photodegradation.[32,33] The quantitative FTIR evidence demonstrates that ester bond degradation is the primary chemical change across all treatments, while UV-vis spectroscopy reveals that electronic structure modifications reflect formation of new chromophoric species and changes in conjugation pathways. The comparative data in Table 6 clearly show that UV irradiation provides the most surface-selective modification (lowest aromatic disruption), while optimal $H_2O_2$ (15%) achieves balanced functionalization, and NaOH hydrolysis uniquely generates carboxylate species through ester cleavage while significantly disrupting extended conjugation. The preserved morphological integrity ensures that improvements in photodegradation performance result from chemical and interfacial changes rather than alterations to pore structure or physical shape. The combination of surface-level chemical modification, preserved bulk polymer integrity, and maintained high-porosity network represents an optimal design for adsorption-assisted photolysis applications.

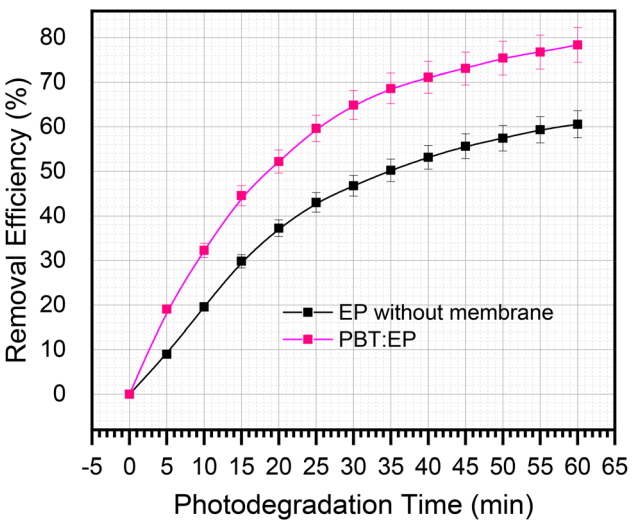


Fig. 6 Comparing EP photodegradation under UV light with and without an unmodified PBT membrane. The PBT membrane enhances EP removal by concentrating the pollutant at the UV-exposed interface, supporting adsorption-assisted photolysis. Data show mean ± SD ($n = 3$).

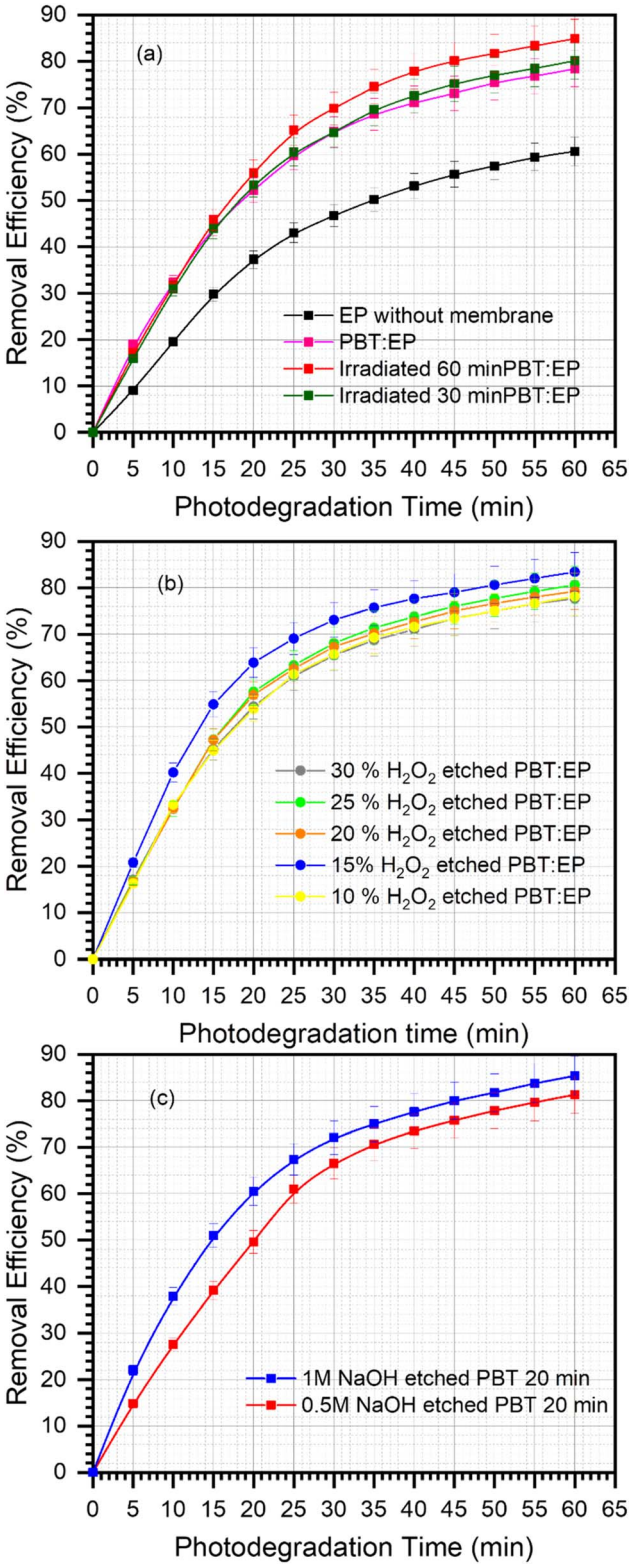


Fig. 7 Time-dependent photodegradation of EP using surface-modified PBT membranes under UV light. (a) EP photodegradation kinetics with and without PBT membranes, where UV pretreatment of PBT for 60 min results in the highest removal efficiency (~85%) due to increased surface polarity and enhanced adsorption of EP at the irradiated interface. (b) Time-dependent EP removal using PBT membranes etched with 10–30% $H_2O_2$ for 30 min, where moderate oxidation (15%) achieves the highest efficiency, while higher concentrations show diminishing returns. (c) Time-dependent EP photodegradation with NaOH-etched PBT membranes (20 min), where a stronger alkaline treatment (1.0 M) results in higher removal efficiency compared to 0.5 M, indicating more effective surface hydrolysis. Data for all panels represent mean ± SD ($n = 3$).

### 3.2. Photodegradation efficiency of EP using surface-modified PBT membranes: investigation of UV, $H_2O_2$, and NaOH treatments in adsorption-assisted photolysis

Before assessing the impact of the additional surface modifications, it is crucial to quantify the baseline contribution of the manufacturer's oxygen-plasma pre-treatment. As established in the control experiments (Fig. 6), the pristine (plasma-treated) PBT membrane achieves an EP removal of approximately 75% in 60 minutes, a significant improvement over the ~60% removal from direct UV photolysis alone. This 15% enhancement is attributed to the initial hydrophilicity and adsorptive capacity imparted by the plasma treatment. Our subsequent surface modifications (UV, $H_2O_2$, and NaOH treatments) were therefore evaluated for their incremental performance gains beyond this 75% benchmark.

This section explores how each surface modification influences EP photodegradation under UV light by comparing removal efficiencies and kinetic patterns. Although PBT lacks inherent photocatalytic activity, it can support adsorption-assisted photolysis, a process where the membrane enhances local pollutant concentration at the UV-exposed interface, thereby improving overall degradation.[43] The aim of surface modification is to increase EP affinity by carefully adding polar functional groups.

UV irradiation introduces small populations of hydroxyl and carbonyl groups, increasing surface polarity and enhancing interactions with EP molecules.[28] $H_2O_2$ etching introduces additional oxygen-containing surface functionalities that enhance EP binding.[44]

NaOH treatment selectively cleaves ester linkages, forming hydroxyl and carboxylate groups that further strengthen adsorption-driven interactions.[45]

Fig. 6 compares EP photodegradation with and without an unmodified PBT membrane under UV light. Even the pristine PBT significantly enhances EP removal compared to UV alone, confirming that the membrane acts as an adsorptive scaffold that concentrates EP at the irradiated interface. This baseline behavior is crucial for understanding the performance improvements from subsequent surface functionalization.

Following this baseline comparison, experiments with UV-treated (60 min), $H_2O_2$-treated (15%, 30 min), and NaOH-treated (1 M, 20 min) PBT membranes showed further improvements in EP degradation efficiency.[46] These enhancements are consistent with moderate yet significant increases in surface polarity, confirmed by FTIR and UV-Vis spectra, which promote stronger EP-surface interactions and boost interfacial reactivity during UV exposure.

**3.2.1. Photodegradation efficiency of EP using UV-irradiated PBT membranes.** This section explores how UV-irradiated PBT membranes influence the photodegradation of

EP under UV light. Although PBT is not naturally photoreactive, its surface can be modified by UV pretreatment to improve adsorption-assisted photolysis, where adsorbed EP molecules break down more quickly due to their closeness to the irradiated surface.

Fig. 7a compares EP removal under four conditions: UV irradiation alone, pristine PBT, and PBT membranes pre-irradiated for 30 and 60 min. UV irradiation of the EP solution without any membrane achieved approximately 60% removal after 60 min, indicating the relative stability of EP and the lack of a reactive interface. Adding a pristine PBT membrane increased removal efficiency to about 75%. This improvement results from PBT's ability to adsorb EP molecules and locally raise their concentration at the UV-irradiated boundary layer, thus enhancing their exposure to photolytic conditions.[27,28]

UV pretreatment of the membrane further improved EP degradation. A 30 min UV exposure resulted in about 80% removal, while the 60 min UV-irradiated membrane achieved the highest efficiency (~85%). These improvements are related to increased surface polarity caused by UV-induced formation of carbonyl and hydroxyl groups, as confirmed by FTIR measurements.[28] The introduction of these polar groups boosts EP adsorption through hydrogen bonding and dipolar interactions while simultaneously enhancing membrane wettability, thereby allowing for more effective interaction at the aqueous interface.

In addition to chemical functionalization, UV exposure can cause slight surface roughening, which may improve interfacial contact and enhance effective photon utilization by promoting light scattering near the membrane surface.[47,48] These effects together strengthen EP–surface interactions and support the adsorption-assisted photolytic pathway.

To create a clear mechanistic framework, we divide the EP degradation process into three distinct contributions.

- Adsorption contribution: polar oxygen-containing functional groups—such as –OH, C═O, and —$COO^-$— on the membrane surface attract EP molecules through hydrogen bonding and electrostatic interactions, forming a localized high-concentration zone at the solid–liquid interface. This process alone (as seen in dark controls) accounts for 8–12% of removal.

- Direct photolysis contribution: UV irradiation (254 nm) breaks bonds in EP molecules through excited-state chemistry. This occurs both in the bulk solution (contributing about 60% to removal in membrane-free controls) and at the membrane interface, where the local concentration is higher.

- ROS-mediated oxidation contribution: UV irradiation of water and dissolved oxygen produces reactive oxygen species (mainly $^{\bullet}OH$ radicals) that attack EP molecules. This process is most effective at the membrane interface because it is close to the ROS generation area and the concentrated EP molecules.

This separation explains why membrane systems achieve 75–86% removal—significantly higher than the sum of individual contributions due to interfacial synergy.

Once EP concentrates at the membrane interface, two simultaneous processes cause its degradation. First, adsorbed EP absorbs incident UV photons, forming an excited state (EP*), which becomes more vulnerable to bond cleavage. Second, UV irradiation of water and dissolved oxygen produces ROS, mainly hydroxyl radicals ($^{\bullet}OH$), known for their role in paraben degradation.[42] These highly reactive radicals attack the excited EP molecules, initiating a series of oxidative reactions. The primary degradation step typically involves breaking the ester bond, producing *p*-hydroxybenzoic acid (PHBA), which then undergoes further oxidation and ring-opening reactions to form $CO_2$, $H_2O$, and smaller organic acids.[49,50]

The mechanistic sequence can be summarized as:

$$EP_{ads} + h\nu \rightarrow EP^*$$

$$EP^* + {}^{\bullet}OH \rightarrow \text{intermediates} \rightarrow CO_2 + H_2O + \text{acids} \quad (4)$$

where EP* denotes the photoexcited state and $^{\bullet}OH$ represents hydroxyl radicals generated under UV irradiation.

This mechanism demonstrates how UV-irradiated PBT membranes speed up EP degradation, even though the polymer does not have inherent photocatalytic properties. By gathering EP molecules near the UV-active zone and the ROS-producing area, the membrane boosts the chance of oxidative attack and shortens the diffusion path between reactants.[51–54] The result is a quicker, more effective degradation process driven by both adsorption and photolysis.

In summary, UV irradiation effectively activates PBT membranes for the interfacial photolytic degradation of EP. Among the tested conditions, the 60 min UV-treated PBT membrane provides the best balance between enhanced adsorption and increased interfacial reactivity, highlighting the significance of surface engineering in developing catalyst-free, polymer-based systems for water purification.

**3.2.2. Photodegradation efficiency of EP utilizing $H_2O_2$-etched PBT membranes.** To assess the effect of oxidative surface activation on EP degradation, PBT membranes were etched in $H_2O_2$ at concentrations ranging from 10% to 30% (v/v) and tested for adsorption-assisted photodegradation under UV light. Fig. 8 and 9 display the performance trends at different concentrations and durations.

Fig. 7b shows the time-dependent EP removal efficiencies for membranes oxidized for 30 min. All $H_2O_2$-treated membranes perform better than pristine PBT because they develop oxygen-containing surface groups that increase hydrophilicity and enhance EP adsorption. Among the tested $H_2O_2$ concentrations, the 15% $H_2O_2$ treatment achieved the highest removal efficiency (~84% at 60 min). Oxidation at this level appears to introduce a beneficial amount of polar carbonyl and hydroxyl groups, which improve EP retention at the UV-irradiated interface.

At higher concentrations (20–30%), EP removal remains better than untreated PBT but does not surpass the performance of the 15% sample. This likely suggests a diminishing return, where increased oxidation does not proportionally enhance reactivity. Over-oxidation may weaken adsorption or cause minor surface changes, limiting the gains. Conversely, 10% $H_2O_2$ provides only modest improvements, consistent with insufficient surface activation.[55,56]

Fig. 8 evaluates the combined impact of $H_2O_2$ concentration and etching time. At 15% $H_2O_2$, removal efficiency consistently increases with time and peaks at 30 min, showing that steady but controlled oxidation improves surface activation. For higher concentrations (20–30%), performance tends to plateau sooner (15–20 min) or slightly decrease at longer durations. This pattern indicates an oxidation threshold, beyond which further exposure does not enhance EP–surface interactions and may slightly reduce adsorption efficiency.[56,57] At shorter etching times (5–10 min), improvements are modest across all concentrations, confirming the need for a minimum oxidation period to achieve sufficient surface polarity.

Overall, the performance trends support the adsorption-assisted photodegradation mechanism observed throughout this study. Oxidative etching improves the membrane's affinity for EP by adding polar functionalities, which increases pollutant concentration at the UV-irradiated surface and enhances interaction with incident light and reactive species in solution. However, excessive oxidation (high concentration or prolonged exposure) can weaken adsorption interactions and reduce the overall beneficial effect.[26,58]

The best balance between functional-group density and surface preservation was reached at 15% $H_2O_2$ for 30 min, yielding the highest EP removal (~84% at 60 min). These findings highlight the importance of controlled oxidative modification in designing polymer membranes that improve photodegradation performance through interfacial, catalyst-free mechanisms.

**3.2.3. Photodegradation efficiency of EP using NaOH-treated PBT membranes.** After oxidative treatments, the impact of alkaline surface modification on EP photodegradation was examined using PBT membranes etched with 0.5 M and 1.0 M NaOH. NaOH hydrolysis selectively breaks surface ester bonds, creating hydroxyl and carboxylate groups that increase hydrophilicity and attract pollutants. Since FTIR and SEM show these changes are confined to the outer polymer layer, NaOH-treated PBT remains structurally intact but chemically active—aligning with the adsorption-assisted photolysis observed in UV and $H_2O_2$-modified samples.

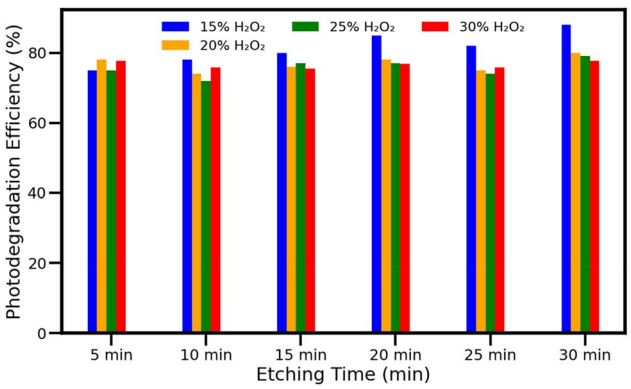


Fig. 8 EP removal efficiency based on $H_2O_2$ concentration and etching time. The best activation occurs at 15% $H_2O_2$ for 30 min. Higher concentrations reach a plateau sooner, indicating an oxidation limit beyond which extra exposure doesn't improve performance.

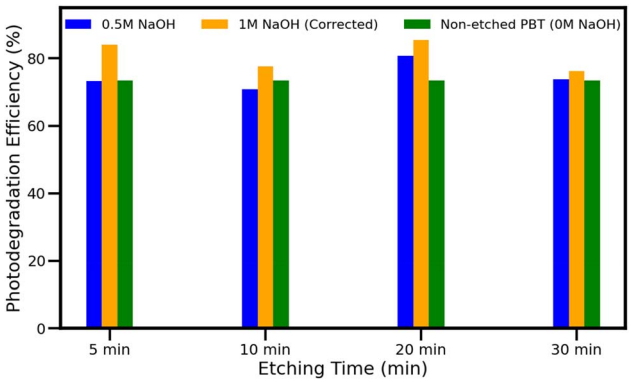


Fig. 9 EP removal efficiency as a function of NaOH etching time for 0.5 M and 1.0 M NaOH. Maximum performance was achieved after 20 min using 1.0 M NaOH. Longer treatment times provided limited improvement, indicating an optimal hydrolysis window.

As shown in Fig. 7c, both alkaline treatments improved EP degradation compared to pristine PBT, confirming that even slight surface hydrolysis enhances EP–surface interactions. After 60 min of UV exposure, the membrane etched with 0.5 M NaOH achieved approximately 81% removal, while 1.0 M NaOH reached about 86%, making it the most effective alkaline condition tested. This improvement correlates with a higher density of hydrophilic groups (–OH, $-COO^-$) generated at higher alkaline concentrations, which promote EP adsorption at the irradiated interface and increase its participation in interfacial photolysis.[59,60]

The combined effect of exposure time and concentration is illustrated in Fig. 9. Throughout all durations, NaOH-treated membranes consistently outperformed pristine PBT, emphasizing the significance of increased surface polarity for adsorption-assisted degradation. For both 0.5 M and 1.0 M NaOH, removal efficiencies improved with etching time, reaching their peak at 20 min, which aligns with the optimal conditions shown in Fig. 9. Beyond this point (20–30 min), performance either plateaued or slightly declined, likely due to over-hydrolysis of the surface layer, which can reduce the number of functional adsorption sites or cause minor surface smoothing that weakens interfacial adhesion.[61]

Similar to the trends seen with UV and $H_2O_2$-modified membranes, the improved performance of NaOH-treated PBT results from the creation of polar, hydrophilic surface sites that attract EP molecules to the membrane–solution interface.

Once adsorbed, EP undergoes the same photodegradation pathway described in Section 3.2.2, involving photoexcitation, ROS attack, and stepwise mineralization.[62] It is important to emphasize that the membrane does not function as a photocatalyst; rather, it serves as an interfacial scaffold that collects EP molecules and enhances their interaction with UV light and photolytically generated ROS. The NaOH-treated membrane does not act as a photocatalyst; instead, it serves as an interfacial scaffold that collects EP molecules and enhances their

interaction with UV light and ROS, similar to the behavior observed in the UV and $H_2O_2$-modified membranes.

Among the tested alkaline conditions, 1.0 M NaOH for 20 min achieved the highest removal efficiency (~86% at 60 min). This shows that controlled alkaline hydrolysis effectively boosts adsorption-assisted photodegradation while preserving the membrane's microstructure. Along with the UV and $H_2O_2$-modified membranes, these results confirm that surface chemistry—rather than morphology—is the main factor driving performance enhancement, and that engineered PBT membranes can serve as scalable, catalyst-free supports for pollutant removal in water treatment systems.

A comparative summary of the optimized photodegradation performance for all three modification strategies is presented in Table 7.

All three surface modifications achieve similar maximum removal efficiencies (84–86%), demonstrating that various surface-engineering strategies can effectively improve membrane performance. The observed 24–26% absolute improvement over UV irradiation alone highlights the important role of interfacial enrichment in enhancing photodegradation. Furthermore, the performance differences among the modified membranes stay within experimental uncertainty (±3%), indicating that the main factor driving improved photodegradation is the increase in surface polarity, not the specific chemical modification pathway used.

To reinforce the mechanistic interpretation outlined earlier, Scheme 2 summarizes the proposed adsorption-assisted photodegradation pathway of EP on the surface-engineered PBT membranes.

Having established the mechanistic basis of EP degradation, the kinetic behavior was analyzed to quantify the influence of surface functionalization on the rate of adsorption-assisted photodegradation.

### 3.3. Kinetic behaviour of EP photodegradation on surface-modified PBT membranes

**3.3.1. Rational and model formulation.** In this catalyst-free system, enhanced EP degradation results from adsorption-assisted photodegradation, where surface-functionalized PBT initially concentrates EP at polar sites (–OH, C═O, $–COO^-$) introduced by UV irradiation, $H_2O_2$ etching, or NaOH hydrolysis. Once adsorbed, EP undergoes photolysis under UV light and oxidative attack by short-lived ROS generated in water.[18,63]

A biphasic kinetic model was used to differentiate between rapid interfacial degradation and slower bulk photolysis.

$$C_t = C_{\text{fast}}e^{-k_1 t} + C_{\text{slow}}e^{-k_2 t} \quad (5)$$

In normalized form, with $C_0 = C_{\text{fast}} + C_{\text{slow}}$:

$$\frac{C(t)}{C_0} = ae^{-k_1 t} + be^{-k_2 t}, \;\; a + b = 1 \quad (6)$$

The associated diagnostic quantities are:

$$r_0 = -\left(\frac{dC}{dt}\right)_{t=0} = k_1 C_{\text{fast}} + k_2 C_{\text{slow}}, \quad (7)$$

$$t_{1/2}{}^{(1)} = \frac{\ln 2}{k_1} \quad (8)$$

$$t_{1/2}{}^{(2)} = \frac{\ln 2}{k_2} \quad (9)$$

The symbol, description, and units for all primary fit parameters, derived diagnostic quantities, and goodness-of-fit metrics are defined in Table 8.

The rapid interfacial pathway explains the quick decline of EP near the membrane surface. Two parameters control this.

- $C_{\text{fast}}$: represents the amount of EP accumulated at the membrane interface. Higher values indicate stronger adsorption, which is directly related to surface functionalization (–OH, C═O, $–COO^-$).

- $k_1$ ($min^{-1}$): the rate at which interface-bound EP undergoes photodegradation. Larger $k_1$ values reflect more efficient interfacial photolysis driven by enhanced UV absorption, improved wettability, and better ROS access.

This phase occurs when surface modification effectively focuses EP at the interface—specifically the improvement observed in UV-irradiated, $H_2O_2$-etched, and NaOH-treated PBT membranes.

The slow bulk pathway describes EP degradation occurring outside the membrane, in the uniform aqueous phase.

- $C_{\text{slow}}$: fraction of EP not significantly interacting with the membrane.

- $k_2$: photolysis rate constant in the bulk solution, typically much smaller than $k_1$ due to lower photon density and reduced ROS availability.

The systems where $C_{\text{fast}} \gg C_{\text{slow}}$ and $k_1 \gg k_2$ exhibit primarily surface-controlled photodegradation, consistent with enhanced EP enrichment and faster interfacial reaction kinetics. However, the model cannot fully separate intrinsic reaction rates from mass-transfer contributions. Diffusion to

Table 7 Comparative summary of EP photodegradation performance under optimized conditions

| Treatment | Optimal conditions | Removal efficiency (60 min) | Enhancement *vs.* UV alone | Enhancement *vs.* pristine PBT | Key kinetic feature |
|---|---|---|---|---|---|
| UV alone | — | 60 ± 2% | — | — | Slow bulk phase dominant |
| Pristine PBT | As received | 75 ± 3% | +15% | — | Moderate interfacial enrichment |
| UV-PBT | 60 min pre-irradiation | 85 ± 3% | +25% | +10% | Highest interfacial enrichment |
| $H_2O_2$-PBT | 15% v/v, 30 min | 84 ± 3% | +24% | +9% | Fastest interfacial kinetics |
| NaOH-PBT | 1.0 M, 20 min | 86 ± 3% | +26% | +11% | Balanced, robust performance |

and from the membrane surface may influence both $C_{fast}$ and $k_1$, and thus the biphasic description should be interpreted as an apparent kinetic decomposition rather than a strict mechanistic partition.

The parameters were extracted using non-linear least squares fitting (Levenberg–Marquardt) with constraints: $k_i > 0$ and $0 \leq a,b \leq 1$.

Replicate measurements were averaged, and inverse-variance weighting was used. The biphasic model accurately represented the behavior of all systems (Fig. 10), and fitting metrics ($R^2$, RMSE) along with 95% confidence intervals are reported in Table 9.

**3.3.2. Extracted parameters and derived metrics.** Table 9 summarizes the kinetic parameters derived from biphasic fitting. Instead of listing the numerical values again, the discussion below emphasizes the mechanistic significance of these parameters—particularly the prominence of the fast, interfacial pathway across all membrane-containing systems and the minimal role of the slow, bulk-photolysis component.

A central observation is that $C_{slow}$ values for the pristine PBT, UV-irradiated PBT, and $H_2O_2$-etched PBT membranes are

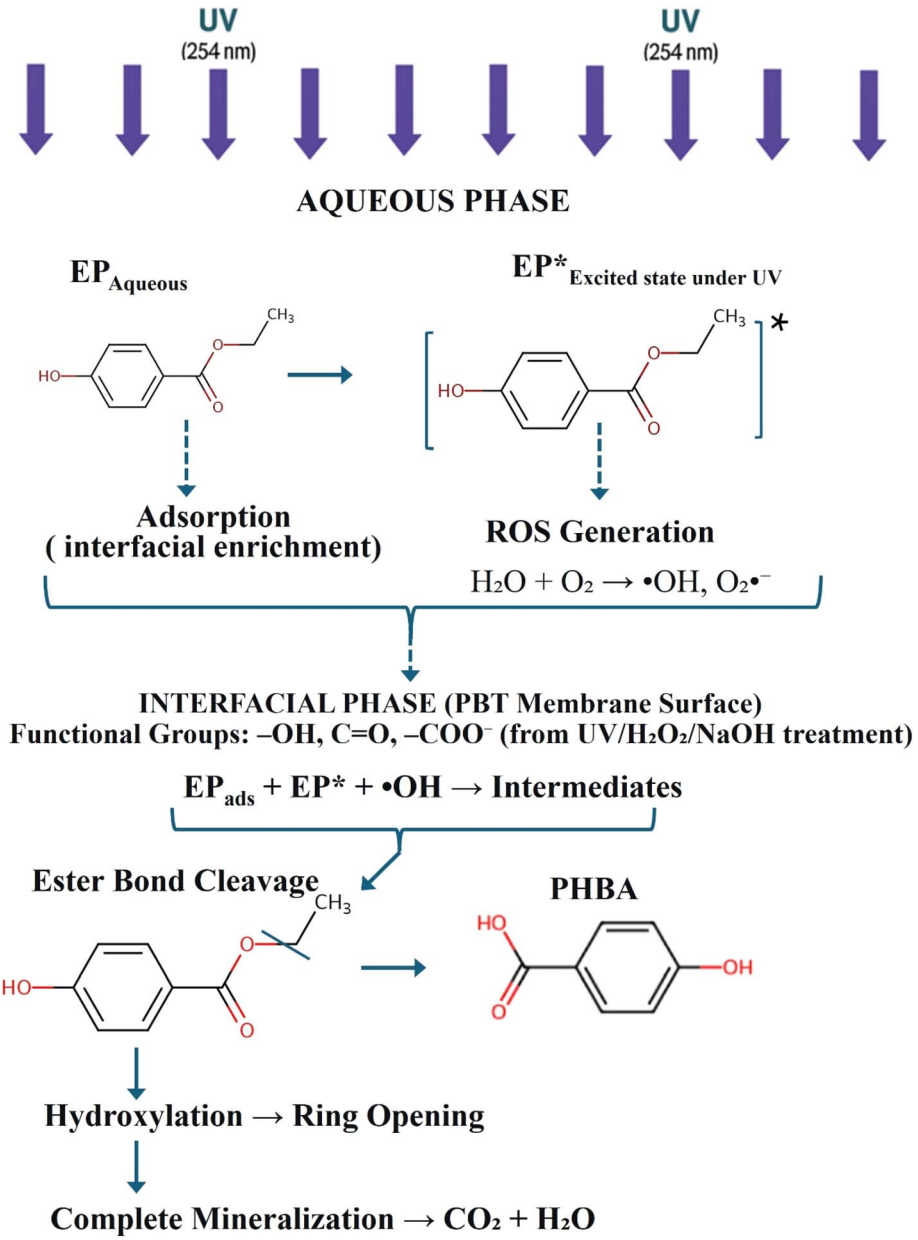


Scheme 2 Proposed mechanism of adsorption-assisted photodegradation of EP on surface-engineered PBT membranes. Oxygenated functional groups (–OH, C═O, $-COO^-$) introduced by UV, $H_2O_2$, or NaOH treatments improve EP adsorption at the membrane–water interface (interfacial enrichment). Under UV irradiation (254 nm), adsorbed EP becomes photoexcited (EP*), while simultaneous ROS generation ($^{\bullet}OH$, $O_2^{\bullet-}$) from water and dissolved oxygen promotes interfacial oxidative attack. Degradation occurs through ester bond cleavage to produce PHBA, followed by hydroxylation, ring opening, and complete mineralization to $CO_2$ and $H_2O$. The biphasic kinetic behavior is evident in the separation between aqueous-phase processes and surface-confined interfacial reactions.

Table 8 Nomenclature for biphasic kinetic model parameters

| Parameter | Description | Units |
|---|---|---|
| **Primary fit parameters** | | |
| $C(t)$ | Concentration of EP at time $t$ | mg $L^{-1}$ |
| $C_0$ | Initial concentration of EP at $t = 0$ | mg $L^{-1}$ |
| $a$ | Fraction of initial EP in the rapid (interfacial) degradation phase | Dimensionless |
| $k_1$ | First-order rate constant for the rapid (interfacial) phase | $min^{-1}$ |
| $b$ | Fraction of initial EP in the slow (bulk) degradation phase (where $a + b = 1$) | Dimensionless |
| $k_2$ | First-order rate constant for the slow (bulk) phase | $min^{-1}$ |
| **Derived diagnostic quantities** | | |
| ${t_{1/2}}^{(1)}$ | Half-life of the rapid (interfacial) phase, calculated as $\ln(2)/k_1$ | min |
| ${t_{1/2}}^{(2)}$ | Half-life of the slow (bulk) phase, calculated as $\ln(2)/k_2$ | min |
| $r_0$ | Initial degradation rate at $t = 0$, calculated as $k_1C_{fast} + k_2C_{slow}$ | mg $L^{-1}$ $min^{-1}$ |
| **Goodness-of-fit metrics** | | |
| $R^2$ | Coefficient of determination | Dimensionless |
| RMSE | Root mean square error | mg $L^{-1}$ |

effectively zero within the fit uncertainty. As a result, the corresponding slow-phase rate constants $k_2$ approach zero and the associated half-lives (${t_1}_/_2^{(2)}$) become non-quantifiable, indicating that degradation is almost entirely governed by the rapid interfacial process, and the fitted model collapses to a single dominant exponential term. The "Not Applicable" entries in Table 9, therefore, reflect the absence of a measurable bulk contribution, not a flaw in the model.

These findings provide strong kinetic evidence supporting the adsorption-assisted photolysis mechanism described earlier. By enriching EP at the solid–liquid interface, surface-functionalized PBT membranes increase the fraction of EP that is simultaneously exposed to UV photons and short-lived ROS. The resulting enhancement in the fast-phase reservoir $C_{fast}$ and the interfacial rate constant $k_1$ explains why membrane-based systems exhibit much faster decay than homogeneous photolysis.

A minor exception is observed for the 1.0 M NaOH-treated membrane, which retains a small but measurable slow component ($k_2 \approx 0.0072$ $min^{-1}$). This should not be seen as a distinct mechanistic regime; instead, it probably indicates incomplete interfacial capture of EP or slight variation in the early-time concentration distribution. Even in this case, the rapid phase still dominates—consistent with interfacial enrichment as the main factor controlling reactivity.

Across all modified membranes, the rapid interfacial pathway primarily determines the observed kinetics. Increasing surface polarity and functional group density (–OH, $–COO^-$, C=O) consistently boosts the fast-phase reservoir and speeds up interfacial reactivity. These effects confirm that the membrane's role is to redirect photodegradation away from the inefficient bulk phase toward a highly reactive interfacial zone where EP is concentrated.

Finally, it should be noted that near-zero $k_2$ values must be interpreted with caution. The 0–60 min experimental window may not capture very slow bulk photolysis; however, this limitation does not alter the overall conclusion that membrane-enabled interfacial processes overwhelmingly dominate EP removal under the conditions studied.

(i) Membrane-based systems are primarily controlled by the rapid interfacial pathway, confirming adsorption as the main driver of enhanced photodegradation.

(ii) Among the modified membranes, $H_2O_2$-etched PBT exhibits the highest fast-phase rate constant ($k_1$), while UV-irradiated PBT shows the largest fast-phase reservoir ($C_{fast}$), reflecting strong EP enrichment at the interface.

 

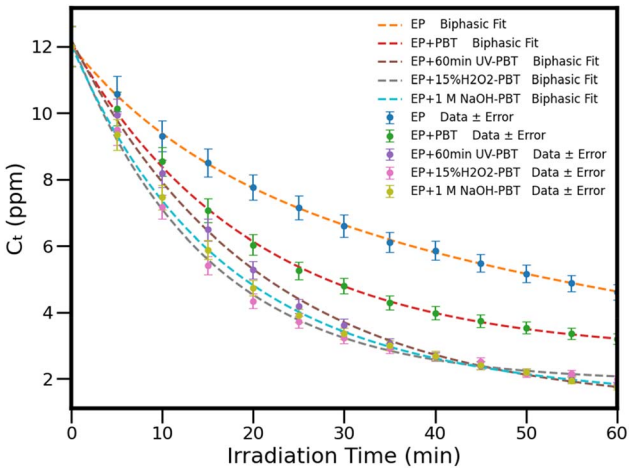


Fig. 10 Kinetic profiles of EP decay (12 mg. $L^{-1}$) under UV for: EP only; EP + pristine PBT; EP + UV-irradiated PBT (60 min); EP + 15% $H_2O_2$-etched PBT (30 min); and EP + 1.0 M NaOH-treated PBT (20 min). Symbols represent experimental data; dashed lines indicate biphasic fits. All treated membranes exhibit a dominant fast interfacial phase with a weaker slow bulk contribution, confirming the kinetic advantage conferred by surface functionalization.

(iii) Near-zero $k_2$ values should be interpreted carefully: the 0–60 min experimental window might not capture extremely slow bulk photolysis. Nonetheless, the data strongly support a degradation mechanism driven by membrane-enabled interfacial processes.

**3.3.3. Comparative trends, mechanistic interpretation, and sensitivity analysis.** The extracted kinetic parameters provide a unified mechanistic picture of how each surface-modification strategy enhances adsorption-assisted photodegradation of EP. Across all membrane-based systems, the rapid interfacial pathway dominates (with $k_2 \rightarrow 0$), demonstrating that modified PBT functions primarily by concentrating EP at a reactive polymer–water interface rather than by facilitating reaction in the aqueous bulk phase.

$C_{fast} \approx 11.01$ mg $L^{-1}$, $t_{1/2}{}^{(1)} \approx 14.11$ min. Among the treatments, UV-PBT (60 min) exhibits the largest fast-phase reservoir ($C_{fast} \approx 11.01$ mg $L^{-1}$) and the highest fraction of fast-phase degradation (~0.90), indicating near-complete reliance on interfacial photolysis. This arises from UV-induced formation of carbonyl and hydroxyl groups that substantially enhance hydrophilicity and EP affinity.[50,64] Despite this strong interfacial enrichment, UV-PBT shows the slowest intrinsic interfacial kinetics among the modified membranes ($t_{1/2}{}^{(1)} \approx 14.11$ min), suggesting that once adsorbed, EP is processed more gradually than on chemically etched surfaces.

In contrast, 15% $H_2O_2$ (30 min) provides the fastest interfacial photodegradation, characterized by the highest rate constant ($k_1 \approx 0.068$ $min^{-1}$) and shortest half-life ($t_{1/2}{}^{(1)} \approx 10.18$ min). It also yields the largest initial degradation rate ($r_0 \approx 0.699$ mg. $L^{-1}$. $min^{-1}$). These results indicate that controlled oxidative etching creates a well-balanced interface: sufficiently oxidized to enhance EP adsorption, yet not over-oxidized to the point of disrupting interfacial reactivity. The fast-phase share

Table 9 Extracted biphasic kinetic parameters ($k_1$, $k_2$, $C_{slow}$, $C_{fast}$) describing the rapid interfacial and slower bulk photodegradation pathways of EP([EP]$_i$ = 12 mg $L^{-1}$). All symbols are defined in Table 8. Values are means from the fit; ±95% are half-widths of 95% confidence intervals from the covariance matrix

| Treatment | $C_{fast}$ (mg $L^{-1}$) | ±95% | $k_1$ ($min^{-1}$) | ±95% | $t_{1/2}{}^{(1)}$ (min) | $C_{slow}$ (mg $L^{-1}$) | ±95% | $k_2$ ($min^{-1}$) | ±95% | $t_{1/2}{}^{(2)}$ (min) | $r_0$ (mg $L^{-1}$ $min^{-1}$) | Fast share | $R^2$ | RMSE (mg $L^{-1}$) |
|---|---|---|---|---|---|---|---|---|---|---|---|---|---|---|
| EP only | 3.78 | 0.98 | 0.0679 | 0.0164 | 10.21 | 8.23 | 1.01 | 0.0098 | 0.0019 | 70.49 | 0.338 | 0.315 | 0.9997 | 0.041 |
| EP + PBT (pristine) | 9.34 | 1.82 | 0.0512 | 0.0108 | 13.53 | 2.77 | 1.88 | 0 | 0.0097 | N/A[a] | 0.479 | 0.771 | 0.9991 | 0.080 |
| EP + UV-PBT (60 min) | 11.01 | 3.22 | 0.0491 | 0.0150 | 14.11 | 1.17 | 3.31 | 0 | 0.0396 | N/A[a] | 0.541 | 0.904 | 0.9984 | 0.127 |
| EP + 15% $H_2O_2$-PBT (30 min) | 10.26 | 1.68 | 0.0681 | 0.0148 | 10.18 | 1.90 | 1.75 | 0 | 0.0154 | N/A[a] | 0.699 | 0.844 | 0.9979 | 0.139 |
| EP + 1.0 M NaOH-PBT (20 min) | 9.52 | 1.48 | 0.0642 | 0.0097 | 10.80 | 2.51 | 1.52 | 0.0072 | 0.0094 | 96.49 | 0.630 | 0.791 | 0.9995 | 0.065 |

[a] The slow phase was negligible or non-quantifiable under these conditions ($k_2 \rightarrow 0$). (i) Membrane-based systems are primarily controlled by the rapid interfacial pathway, confirming adsorption as the main driver of enhanced photodegradation. (ii) Among the modified membranes, $H_2O_2$-etched PBT exhibits the highest fast-phase rate constant ($k_1$), while UV-irradiated PBT shows the largest fast-phase reservoir ($C_{fast}$), reflecting strong EP enrichment at the interface. (iii) Near-zero $k_2$ values should be interpreted carefully: the 0–60 min experimental window might not capture extremely slow bulk photolysis. Nonetheless, the data strongly support a degradation mechanism driven by membrane-enabled interfacial processes.

(~0.84) confirms that degradation remains overwhelmingly interfacial.

NaOH-treated PBT (1.0 M, 20 min) displays a robust interfacial response, with a large fast-phase reservoir ($C_{fast}$ ≈ 9.52 mg $L^{-1}$) and a rapid interfacial rate ($k_1$ ≈ 0.064 $min^{-1}$). It is the only treatment exhibiting a small but measurable slow component ($k_2$ ≈ 0.0072 $min^{-1}$) likely reflecting incomplete EP capture or slight variations in surface morphology after alkaline hydrolysis. Even so, the interfacial pathway clearly dominates, and NaOH-PBT achieves one of the highest overall degradation efficiencies (~86%).

For comparison, pristine PBT enhances EP at the interface but exhibits weaker interfacial kinetics, while EP alone shows a significant slow-phase contribution, highlighting the importance of the membrane in directing degradation toward the faster interfacial regime.

Overall, the comparative kinetic analysis shows that each modification improves a different aspect of the adsorption–photolysis process.

- UV pretreatment maximizes interfacial pollutant loading (high $C_{fast}$).

- $H_2O_2$ etching maximizes the intrinsic interfacial reaction rate (high $k_1$).

- NaOH etching provides a balanced and stable interfacial environment with a distinctive kinetic profile.

Together, these trends confirm that controlled oxidation transforms PBT into a highly effective, catalyst-free interfacial platform capable of concentrating pollutants and accelerating their photochemical degradation. The sensitivity analysis supports these conclusions. For UV treatment, the disappearance of the slow component and the rise in the fast-phase fraction directly correspond to approximately 85% removal efficiency.

For $H_2O_2$ treatment, the kinetics clearly identify 15% for 30 min as the optimal condition; stronger etching (20–30%) produces over-oxidation that reduces $C_{fast}$ and lowers efficiency. For NaOH treatment, 1.0 M for 20 min gives consistent improvements; longer etching confers no benefit and may slightly decrease performance due to over-hydrolysis.

A key mechanistic insight is that moderate oxidation creates the most effective interfacial surfaces, while excessive chemical or photochemical modification can passivate reactive groups or damage the microtexture needed for efficient adsorption. Kinetically, these effects appear as reduced fast-phase contributions and higher residual pollutant levels.

Finally, the main limitation of the biphasic framework is its inability to distinguish intrinsic interfacial reaction rates from transport-related contributions within the aqueous boundary layer. Although adsorption-assisted photodegradation inherently couples mass-transfer and surface reaction steps, the biphasic kinetic model captures the dominant trends but cannot fully resolve their individual contributions. The biphasic kinetic model provides quantitative support for the conceptual framework outlined in Section 3.2.2: the rapid phase ($k_1$) captures the combined effect of interfacial processes (direct photolysis and ROS-mediated attack on adsorbed EP), while the negligible $k_2$ values confirm that bulk-phase photolysis becomes insignificant in membrane-containing systems. While this does not diminish the mechanistic conclusions, future studies varying photon flux, hydrodynamic conditions, or membrane geometry could help clarify these influences. In summary, the biphasic kinetic analysis provides three key quantitative insights:

- Mechanistic shift: membrane incorporation raises the fast-phase fraction from 31.5% (EP alone) to 77–90% (membrane systems), confirming that surface functionalization shifts degradation from inefficient bulk photolysis to faster interfacial pathways.

- Treatment-specific enhancements: UV pretreatment optimizes pollutant loading ($C_{fast}$: 3.78 → 11.01 mg $L^{-1}$, +191%); $H_2O_2$ etching optimizes reaction kinetics ($k_1$: 0.0512 → 0.0681 $min^{-1}$, +33% compared to pristine); NaOH hydrolysis provides balanced improvements ($C_{fast}$: 9.52 mg $L^{-1}$; $k_1$: 0.0642 $min^{-1}$).

- Interfacial dominance: for UV, $H_2O_2$, and NaOH-modified membranes, the contribution from the slow phase ($k_2$) becomes negligible or unmeasurable, indicating that over 95% of EP degradation takes place at the functionalized interface rather than in bulk solution.

These quantitative metrics clearly show that surface-engineered PBT membranes act as adsorptive-concentrating interfaces that speed up photodegradation through interfacial enrichment rather than catalytic activity.

Extending the analysis to pollutants with different hydrophobicity or electronic structures would also test the generality of the adsorption–photolysis mechanism and further validate controlled surface oxidation as a strategy for membrane-assisted water treatment.

# 4. Conclusion

This study demonstrates the feasibility of a catalyst-free, adsorption-assisted photodegradation method for removing ethylparaben (EP) using surface-engineered PBT nonwoven membranes. The increased degradation results solely from interfacial enrichment that speeds up natural photolytic breakdown—without embedded semiconductor photocatalysts.

Three surface-modification strategies (UV irradiation, $H_2O_2$ oxidation, NaOH hydrolysis) were quantitatively evaluated. Spectroscopic analyses confirmed introduction of oxygen-rich functional groups (–OH, C═O, $–COO^-$) with treatment-specific efficiencies: UV reduced ester carbonyl by 76.9% (60 min); 30% $H_2O_2$ achieved 99.8% carbonyl reduction; 1 M NaOH produced 87.4% carbonyl reduction with carboxylate formation. SEM confirmed preservation of microfibrous structure (79–90% porosity) across all treatments.

Under optimized conditions, modified membranes achieved removal efficiencies of 84% (15% $H_2O_2$, 30 min), 85% (UV, 60 min), and 86% (1.0 M NaOH, 20 min)—representing a 24–26% absolute improvement over UV photolysis alone (60%).

Biphasic kinetic analysis revealed that surface modification shifts degradation from the bulk phase to the interface. The fast-phase fraction increased from 31.5% (EP alone) to 77–90% (membrane systems), with the slow-phase contribution ($k_2$)

 

becoming negligible. UV-PBT maximized interfacial enrichment ($C_{fast}$: 11.01 mg $L^{-1}$; 90% interfacial degradation); $H_2O_2$-PBT maximized reaction rate ($k_1$: 0.068 $min^{-1}$; $t_{1/2}^{(1)}$: 10.18 min); NaOH-PBT achieved balanced performance (86% removal).

Future work should include: (i) TOC and GPC analysis to quantify potential leachates; (ii) testing non-plasma-treated PBT to isolate activation effects; (iii) demonstrating the long-term durability and reusability of the membranes under continuous-flow conditions; (iv) exploring emerging contaminants with varying hydrophobicity. Furthermore, a techno-economic assessment should be conducted to evaluate the true scalability and practical viability of this approach for tertiary water treatment. The practical application is envisioned as a tertiary treatment step for persistent micropollutants in pre-treated effluent. In conclusion, controlled surface oxidation transforms standard PBT nonwovens into effective, catalyst-free purification interfaces, achieving 86% EP removal through a quantitatively validated adsorption-assisted photolysis mechanism.

## Conflicts of interest

There are no conflicts to declare.

## Data availability

The data that support the findings of this study are available from the corresponding author upon reasonable request.

## Acknowledgements

The Researchers would like to thank the Deanship of Graduate Studies and Scientific Research at Qassim University for financial support (QU-APC-2026).

## References

1 M. Gmurek, J. F. Gomes, R. C. Martins and R. M. Quinta-Ferreira, *Environ. Sci. Pollut. Res.*, 2019, **26**, 37174–37192, DOI: 10.1007/s11356-019-06705-7.
2 M. T. Penrose and G. P. Cobb, *Water Environ. Res.*, 2022, **94**, e10705, DOI: 10.1002/wer.10705.
3 H. Arfaeinia, Z. Asadgol, B. Ramavandi, S. Dobaradaran, R. R. Kalantari, Y. Poureshgh, S. Sahebi, *et al.*, *Environ. Geochem. Health*, 2022, **44**, 4499–4521, DOI: 10.1007/s10653-022-01205-z.
4 C. Haman, X. Dauchy, C. Rosin and J.-F. Munoz, *Water Res.*, 2015, **68**, 1–11, DOI: 10.1016/j.watres.2014.09.030.
5 M. A. Alvarez, M. Ruidíaz-Martínez, G. Cruz-Quesada, M. V. López-Ramón, J. Rivera-Utrilla, M. Sanchez-Polo and A. J. Mota, *Chem. Eng. J.*, 2020, **379**, 122334, DOI: 10.1016/j.cej.2019.122334.
6 K. Vellingiri, V. Choudhary, D. W. Boukhvalov and L. Philip, *ACS ES&T Water*, 2022, **2**, 1475–1499, DOI: 10.1021/acsestwater.2c00087.
7 P. Li, R. Miao, P. Wang, F. Sun and X. Y. Li, *Chem. Eng. J.*, 2021, **426**, 131263, DOI: 10.1016/j.cej.2021.131263.
8 X. Li, S. Wang, B. Xu, X. Zhang, Y. Xu, P. Yu and Y. Sun, *Chem. Eng. J.*, 2022, **441**, 136074, DOI: 10.1016/j.cej.2022.136074.
9 P. C. Zadra Filho, Synthesis of carbon nanotube composite membranes for catalytic wet peroxide oxidation of emerging contaminants, Master's thesis, Instituto Politécnico de Bragança, 2024, https://hdl.handle.net/10198/30872.
10 M. N. Subramaniam, P. S. Goh, D. Kanakaraju, J. W. Lim, W. J. Lau and A. F. Ismail, *Environ. Sci. Pollut. Res.*, 2022, **29**, 12506–12530, DOI: 10.1007/s11356-021-14676-x.
11 I. F. Vankelecom, *Chem. Rev.*, 2002, **102**, 3779–3810, DOI: 10.1021/cr0103468.
12 C. Chen, L. Lu, L. Fei, J. Xu, B. Wang, B. Li and H. Lin, *Sci. Total Environ.*, 2023, **904**, 166220, DOI: 10.1016/j.scitotenv.2023.166220.
13 I. Ibrahim, A. M. Elseman, H. Sadek, E. M. Eliwa, M. S. Abusaif, P. Kyriakos, T. M. Salama, *et al.*, *Catalysts*, 2025, **15**, 528, DOI: 10.3390/catal15060528.
14 H. S. Zakria, M. H. D. Othman, R. Kamaludin, S. H. S. A. Kadir, T. A. Kurniawan and A. Jilani, *RSC Adv.*, 2021, **11**, 6985–7014, DOI: 10.1039/d0ra10964a.
15 W. J. Lau, C. S. Ong, N. A. H. M. Nordin, N. A. A. Sani, N. M. Mokhtar, R. Jamshidi Gohari and A. Fauzi Ismail, in *Surface Treatments for Biological, Chemical, and Physical Applications*, Wiley-VCH, 2017, ch. 4, pp. 115–180, DOI: DOI: 10.1002/9783527698813.ch4.
16 S. S. Ray, S. S. Chen, C. W. Li, N. C. Nguyen and H. T. Nguyen, *RSC Adv.*, 2016, **6**, 85495–85514, DOI: 10.1039/c6ra14952a.
17 A. Safri, A. J. Fletcher, R. Safri and H. Rasheed, *Molecules*, 2022, **27**, 8483, DOI: 10.3390/molecules27238483.
18 L. Wang, Y. Chen, B. Chen and J. Yang, *J. Hazard. Mater.*, 2021, **404**, 124040, DOI: 10.1016/j.jhazmat.2020.124040.
19 M. J. Silva, R. Alves, T. Chichorro, P. Alves, P. Ferreira, R. C. Martins and J. Gomes, *Sep. Purif. Technol.*, 2025, **354**, 129048, DOI: 10.1016/j.seppur.2024.129048.
20 J. Gomes, B. Maniezo, P. Alves, P. Ferreira and R. C. Martins, *J. Water Process Eng.*, 2022, **46**, 102458, DOI: 10.1016/j.jwpe.2021.102458.
21 A. R. Pereira, I. B. Gomes, M. Harir, L. Santos and M. Simões, *Chem. Eng. J.*, 2024, **498**, 155129, DOI: 10.1016/j.cej.2024.155129.
22 C. R. Derisso, C. M. E. Pompei, M. Spadoto, T. da Silva Pinto and E. M. Vieira, *Water, Air, Soil Pollut.*, 2020, **231**, 468, DOI: 10.1007/s11270-020-04835-0.
23 R. N. Baxi, S. U. Pathak and D. R. Peshwe, *Polym. J.*, 2011, **43**, 801–808, DOI: 10.1038/pj.2011.69.
24 P. Mane, A. J. Keche, S. Chopra and K. Pande, *J. Appl. Polym. Sci.*, 2024, **141**, e55902, DOI: 10.1002/app.55902.
25 A. Rivaton, F. Serre and J. L. Gardette, *Polym. Degrad. Stab.*, 1998, **62**, 127–143, DOI: 10.1016/S0141-3910(97)00271-1.
26 P. Gijsman, G. Meijers and G. Vitarelli, *Polym. Degrad. Stab.*, 1999, **65**, 433–441, DOI: 10.1016/S0141-3910(99)00033-6.
27 H. Liu, Y. Zheng, P. V. Gurgel and R. G. Carbonell, *J. Membr. Sci.*, 2013, **428**, 562–575, DOI: 10.1016/j.memsci.2012.09.047.
28 C. Salvagnini, A. Roback, M. Momtaz, V. Pourcelle and J. Marchand-Brynaert, *J. Biomater. Sci., Polym. Ed.*, 2007, **18**, 1491–1516, DOI: 10.1163/156856207794761934.

29 M. F. Zaki, E. K. Elmaghraby and A. B. Elbasaty, *J. Adhes. Sci. Technol.*, 2016, **30**, 443–457, DOI: 10.1080/01694243.2015.1105123.
30 R. Neuman, *Organic Chemistry*, Prentice Hall, 2004, ch. 13, pp. 3–33.
31 F. Dai, Q. Zhuang, G. Huang, H. Deng and X. Zhang, *ACS Omega*, 2023, **8**, 17064–17076, DOI: 10.1021/acsomega.3c01336.
32 R. Zhong, Z. He, X. Zhang, D. Han, H. Wang and J. Liu, *J. Biomed. Mater. Res., Part A*, 2021, **109**, 1955–1966, DOI: 10.1002/jbm.a.37188.
33 D. Hetemi and J. Pinson, *Chem. Soc. Rev.*, 2017, **46**, 5701–5713, DOI: 10.1039/c7cs00150a.
34 S. Giraldo-Narcizo, A. Guerrero and A. M. Sanchez-Pérez, *ChemBioChem*, 2025, **26**, e202500004, DOI: 10.1002/cbic.202500004.
35 C. Adina, N. Ş. Mariana, M. Ioana, C. Tănasie and M. Micläu, *Rev. Roum. Chim.*, 2017, **62**, 531–538.
36 I. Donelli, G. Freddi, V. A. Nierstrasz and P. Taddei, *Polym. Degrad. Stab.*, 2010, **95**, 1542–1550, DOI: 10.1016/j.polymdegradstab.2010.06.011.
37 A. Krasiński, Ł. Sołtan and J. Kacprzyńska-Gołacka, *Sep. Purif. Technol.*, 2020, **236**, 116254, DOI: 10.1016/j.seppur.2019.116254.
38 A. V. Mitrofanov, O. V. Karban, A. Sugonyako, A. E. Dudkina, I. A. Schelokov and V. V. Polyakov, *J. Surf. Invest.*, 2009, **3**, 519–526, DOI: 10.1134/S1027451009040065.
39 A. Morgan, M. Cocca, K. Vega, A. Fleischer, S. K. Gupta and M. Mehan, *J. Adhes. Sci. Technol.*, 2017, **31**, 2542–2554, DOI: 10.1080/01694243.2017.1308994.
40 J. L. Gardette, A. Rivaton and S. Therias, in *Photochemistry and Photophysics of Polymer Materials*, ed. N. S. Allen, John Wiley & Sons, 2010, ch. 15, pp. 569–601.
41 S. Kushwaha, V. C. Avadhani and R. P. Singh, *Adv. Mater. Lett.*, 2014, **5**, 272–279, DOI: 10.5185/amlett.2014.10533.
42 Y. Nosaka and A. Y. Nosaka, *Chem. Rev.*, 2017, **117**, 11302–11336, DOI: 10.1021/acs.chemrev.7b00161.
43 N. S. Allen, *Chem. Soc. Rev.*, 1986, **15**, 373–404, DOI: 10.1039/CS9861500373.
44 T. Easton, V. Koutsos and E. Chatzisymeon, *J. Environ. Chem. Eng.*, 2022, **10**, 109057, DOI: 10.1016/j.jece.2022.109057.
45 D. J. Miller, D. R. Dreyer, C. W. Bielawski, D. R. Paul and B. D. Freeman, *Angew. Chem., Int. Ed.*, 2016, **55**, 13580–13598, DOI: 10.1002/anie.201601509.
46 H. Rho, S. J. Im, O. Alrehaili, S. Lee, A. Jang, F. Perreault and P. Westerhoff, *Environ. Sci. Technol.*, 2021, **55**, 6984–6994, DOI: 10.1021/acs.est.0c07844.
47 Y. Cao, P. Xu, W. Yang, X. Zhu, W. Dong, M. Chen and P. Ma, *Composites, Part B*, 2021, **205**, 108510, DOI: 10.1016/j.compositesb.2020.108510.
48 X. Liu, L. Wang, X. Zhou, X. He, M. Zhou, K. Jia and X. Liu, *J. Phys. Chem. Solids*, 2021, **154**, 110094, DOI: 10.1016/j.jpcs.2021.110094.
49 S. Donkor, *Photoconversion of Endocrine Disruptors (Parabens) Using Zinc Oxide Photocatalyst, Doctoral Dissertation*, University of Cape Coast, 2020, https://ir.ucc.edu.gh/xmlui/bitstream/handle/123456789/4830/DONKOR%202020.pdf.
50 Z. Qiu, F. Wei, J. Sun, Y. Niu, Q. Mei, B. Wei and M. He, *J. Phys. Chem. A*, 2020, **124**, 10967–10976, DOI: 10.1021/acs.jpca.0c09207.
51 S. Yang, Y. Wang, S. Lin, J. Fan, C. Liu and X. Yan, *Chemosphere*, 2018, **191**, 17–22, DOI: 10.1016/j.chemosphere.2017.10.019.
52 Y. Wu, M. Chen, H. J. Lee, M. A. Ganzoury, N. Zhang and C. F. de Lannoy, *ACS ES&T Eng.*, 2022, **2**, 1574–1598, DOI: 10.1021/acsestengg.2c00201.
53 J. H. Kim, P. K. Park, C. H. Lee and H. H. Kwon, *J. Membr. Sci.*, 2008, **321**, 190–198, DOI: 10.1016/j.memsci.2008.04.055.
54 Z. Zhou, J. Song, L. Nie and X. Chen, *Chem. Soc. Rev.*, 2016, **45**, 6597–6626, DOI: 10.1039/C6CS00271D.
55 G. Stark, *J. Membr. Biol.*, 2005, **205**, 1–16, DOI: 10.1007/s00232-005-0753-8.
56 Y. Xu, W. Lin, D. Yuan, S. Chen, F. Li, Y. Long, C. He, W. Zhao and C. Zhao, *J. Mater. Sci. Technol.*, 2022, **124**, 76–85, DOI: 10.1016/j.jmst.2022.01.028.
57 C. S. Gittleman, F. D. Coms and Y.-H. Lai, in *Polymer Electrolyte Fuel Cell Degradation*, ed. M. M. Mench, E. C. Kumbur and T. N. Veziroglu, Academic Press, 2011, pp. 15–46.
58 P. P. Vaughan and N. V. Blough, *Environ. Sci. Technol.*, 1998, **32**, 2947–2953, DOI: 10.1021/es9710417.
59 G. Zhang, H. Meng and S. Ji, *Desalination*, 2009, **242**, 313–324, DOI: 10.1016/j.desal.2008.05.010.
60 M. R. Puhan, B. Sutariya and S. Karan, *J. Membr. Sci.*, 2022, **661**, 120887, DOI: 10.1016/j.memsci.2022.120887.
61 S. M. Aldebasi, H. Tar, A. S. Alnafisah, H. Salmi-Mani, N. Kouki, F. M. Alminderej and J. Lalevée, *Polymers*, 2023, **15**, 3378, DOI: 10.3390/polym15163378.
62 J. Lincho, J. Gomes and R. C. Martins, *Appl. Sci.*, 2021, **11**, 3556, DOI: 10.3390/app11083556.
63 W. J. Cooper, R. G. Zika, R. G. Petasne and J. M. C. Plane, *Environ. Sci. Technol.*, 1988, **22**, 1156–1160, DOI: 10.1021/es00175a004.
64 S. Gligorovski, R. Strekowski, S. Barbati and D. Vione, *Chem. Rev.*, 2015, **115**, 13051–13092, DOI: 10.1021/cr500310b.